



Nonlinear vibration analysis of vortex-induced vibrations in overhead power lines with nonlinear vibration absorbers

Sunit K. Gupta · Arun L. Malla · Oumar R. Barry 

Received: 16 June 2020 / Accepted: 17 November 2020
© Springer Nature B.V. 2021

Abstract Vortex-induced vibrations are one of the major factors in fatigue failure of power transmission lines and can be mitigated using vibration absorbers in the form of Stockbridge dampers. Since power transmission lines play an important role in modern infrastructure, a thorough understanding of the nonlinear dynamical interactions between conductors, dampers, and wind forces is crucial. Although different nonlinear models exist for conductor vibration with attached dampers or under wind force, no work combines all these nonlinearities in a single model and examines the dynamics of the conductor along with dampers. In an attempt to fill this gap, this work combines the nonlinearities from the mid-plane stretching of the conductor, equivalent cubic stiffness of the Stockbridge damper, and fluctuating lift force modeled as a Van der Pol oscillator in a single model to investigate the nonlinear vortex-induced vibrations. In this work, the conductor is modeled as a simply supported beam and the Stockbridge damper as a mass–spring–damper–mass system with a combination of cubic and linear stiffness. The governing equations of motion are solved analytically using the method of multiple scales for the case of primary resonance between the fluctuating lift-force and conductor. Analytical findings are further validated by comparing against the numerical integra-

tion of a reduced-order system, and the results show an excellent match. The analysis is extended by conducting a parametric study to investigate the effect of different system parameters on the frequency response curves. These findings are promising and further provide a direction to design an optimal vibration absorber.

Keywords Nonlinear vibration · The method of multiple scale · Wake oscillator

1 Introduction

The use of suspended cables can be found in numerous engineering applications due to their flexible structure and capability of transmitting forces or signals across vast distances. One significant application of suspended cables, also known as conductors, is in overhead power transmission lines, which play an essential role in modern infrastructure. Any failure of power transmission lines causes not only discomfort in daily life but also a substantial economic loss to power industries. Due to their long flexible structure with low structural damping, power transmission lines are highly susceptible to vortex-induced vibrations or VIV, which play a crucial role in the fatigue failure of the power transmission cables/conductors. Therefore, it is necessary to develop a complete understanding of cable/conductor dynamics under various circumstances during VIV; this is the focus of the current work.

S. K. Gupta · A. L. Malla · O. R. Barry (✉)
Department of Mechanical Engineering, Virginia Tech,
Blacksburg, Virginia 24061, USA
O. R. Barry
e-mail: obarry@vt.edu

VIV is driven by periodic vortex shedding that occurs due to cross-flow past a bluff cylindrical body [1]. When the frequency of vortex shedding is close enough to the natural frequency of the body, primary resonance occurs, which further leads to potential instability (large amplitude oscillations) in the system [2]. Although in the case of suspended cables, the maximum amplitude of these VIV is on the order of magnitude of the cable diameter, their high-frequency results in the accumulation of fatigue damage on the clamped ends of the conductor and eventually leads to fatigue failure [3–6]. This failure is commonly mitigated by installing Stockbridge dampers on the conductors near the clamps at either end. These passive dampers can reduce or even eliminate conductor vibrations, but their performance depends on positioning, the properties of both conductor and damper [7], and cable-wind interaction. The response of a cable/conductor under VIV with dampers or other in-span fittings (e.g., spacers, suspension clamps, aircraft warning spheres) has been previously studied using several methods such as the energy balance method, the method of impedance, matrix transfer method, the statistical method, and the multi-physics approach [8–17]. However, only the energy balance method and the method of impedance reflect the complex coupling between the conductor and damper dynamics and hence, are the most widely used methods for analysis. Also, it should be noted that the dynamic analyses mentioned above ignore the nonlinearity in the primary system of conductor and dampers, making them incapable of thoroughly describing the system's response under all circumstances. Therefore, it is necessary to include all possible sources of nonlinearity in the system to understand the dynamics of the system completely.

In the existing literature, the conductor is modeled as a Euler–Bernoulli beam. In contrast, Stockbridge dampers have been modeled as a concentrated force [7], another Euler–Bernoulli beam [4,5], or an equivalent mass–spring–damper–mass system [6]. One of the primary sources of nonlinearity in the system stems from the mid-plane stretching of a cable with immovable ends. Also, in the attached damper, there exists a cubic nonlinearity from the equivalent stiffness of the spring–mass system. The system with these nonlinearities has been widely studied in the literature. For the sake of completeness, some of the pioneering works are summarized here. Dowell's model of a nonlinear Euler–Bernoulli beam with a spring-mass

system included the mid-plane stretching nonlinearity [18] and was expanded by Pakdemirli and Nayfeh to add the cubic nonlinearity [19]. This model was extended to include axial tension and multiple mass–spring–damper systems by Barry et al. [20] and Bukhari and Barry [21].

We emphasize that in the studies mentioned in the preceding paragraph, the fluid–structure interaction in the form of VIV lift force, if included, is modeled as a sinusoidal force, and no nonlinearity has been considered in fluid-structure interaction. It has been noticed that for stationary bodies, lift force can be well approximated using a sinusoidal term [1]. However, for moving bodies such as stretching sheets, stretching cylinders, oscillating plates, rotating disks, this approximation does not hold any longer, and more robust models and methods are required to represent fluid–structure interaction and explore the coupled dynamics, respectively [22–26]. Due to limited understanding of the mechanisms of vortex shedding caused by flow around a body [27–29], researchers have employed different models for nonlinear oscillators, such as the Van der Pol oscillator, to represent the fluctuating cross-flow (lift) force on a structure [30–32]. It should be noted that these models were chosen based solely on the observed similarity of the vortex shedding and nonlinear oscillators, not due to any connection of the oscillator equations with fluid dynamics. However, they have shown a good agreement with experimental data and have been used to gain valuable insights into VIV systems [31–34].

One notable trait of VIV is the lock-in phenomenon, in which the frequency of vortex shedding deviates from expected values and approaches the natural frequency of the body oscillating within the fluid. Instead of following the Strouhal law, which dictates that it varies with flow velocity, the shedding frequency will “lock on” to that of the vibrating body, thus coupling the dynamics of vortex shedding and structural vibration [35]. This phenomenon leads to the resonance of vortex-induced vibrations, increasing the vortex strength and fluid forces [36]. Various aspects of lock-in have been studied in detail [36–39]. However, the relevance of lock-in to this paper is mainly to establish the case of primary resonance.

In a review of prior work, it becomes evident that while the intensive study has been performed for a nonlinear cable-damper model with sinusoidal lift force or a cable with a nonlinear model of lift force [40–43], there are no studies combining all sources of nonlin-

earity to analyze the response of the system. In this work, we attempt to fill this gap by considering the nonlinear cable-damper system coupled with a nonlinear model of lift force. Following the above conventions, the conductor is modeled as an Euler–Bernoulli beam with several attached mass–spring–damper–mass systems representing Stockbridge dampers. Forces on the conductor include pretension and vortex-induced lift force modeled as a Van der Pol oscillator. The method of multiple scales (MMS) is used for the case of primary resonance, and an approximate analytical solution is obtained for the coupled weakly nonlinear differential equations. Parametric studies are conducted to examine the effect of different system parameters on the frequency response curves to get a complete understanding of system dynamics under different circumstances. The rest of the paper is organized as follows. In Sect. 2, the complete mathematical model of cable/conductor vibration is presented. This section includes a brief description of the Van der Pol oscillator for the lift-force model, along with the non-dimensionalization of the governing equation of motions. Linear and nonlinear analysis of the system, using the method of multiple scales, are presented in Sect. 3. Results from the nonlinear analysis, along with parametric studies, are presented in Sect. 4. In Sect. 5, some conclusions are drawn from the findings of this analysis.

2 Mathematical formulation

A schematic of a cable/conductor with a pair of attached Stockbridge dampers is shown in Fig. 1. As mentioned earlier, the conductor is modeled as an Euler–Bernoulli beam, whereas each Stockbridge damper is represented by a mass–spring–damper–mass system with equivalent properties. In the schematic, L is the length of cable/conductor, EI is the flexural rigidity of cable, EA is the axial rigidity of cable, m is the mass per unit length of cable, and D is the diameter of cable. Each equivalent p^{th} damper has in-span mass M_{cp} , suspended mass M_{dp} , linear stiffness K_p , cubic nonlinear stiffness q_p , and dashpot damping coefficient C_{dp} . The beam is also subjected to a pretension T and vortex-induced lift force $F_L(x, t)$. The surrounding fluid flows perpendicular to the beam’s axis with a velocity of V_f and a density ρ_f . For this system, the beam’s axial coordinate is denoted by x , and accordingly, the position of a Stockbridge damper along the beam in the left-end

reference frame is denoted x_{sp} . Note that the addition of n number of dampers in the cable divides the span into $n + 1$ segments and hence, the cross-flow (transverse) beam displacement of segment i is denoted by $W_i(x, t)$ and the displacement of M_{dp} is denoted by $V_p(t)$. The notations $()$ and prime $()'$ represent temporal and spatial derivatives, respectively.

Accordingly, the kinetic energy (KE), and potential energy (PE), of the system are [21]

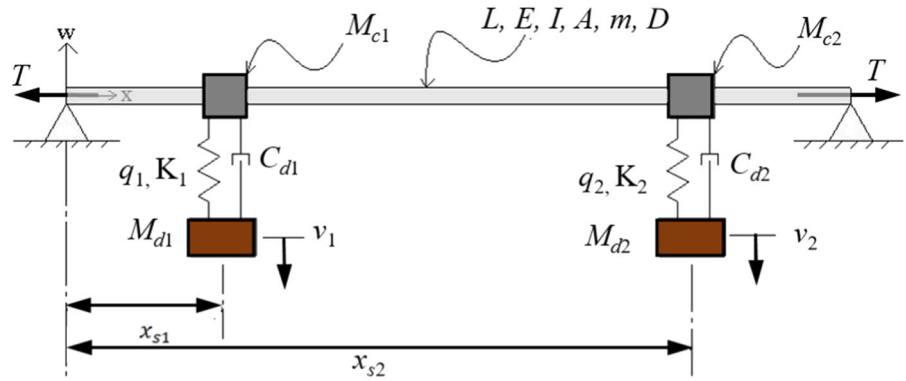
$$\begin{aligned}
 KE &= \sum_{i=0}^n \int_{x_{si}}^{x_{s(i+1)}} m \dot{W}_{i+1}^2 dx \\
 &+ \frac{1}{2} \sum_{i=1}^n M_{ci} \dot{W}_i(x_{si}, t)^2 \\
 &+ \frac{1}{2} \sum_{i=1}^n M_{di} \dot{V}_i(t)^2. \tag{1}
 \end{aligned}$$

$$\begin{aligned}
 PE &= \frac{1}{2} \sum_{i=0}^n \int_{x_{si}}^{x_{s(i+1)}} EI(W''_{i+1})^2 dx \\
 &+ \frac{1}{2} \sum_{i=0}^n \int_{x_{si}}^{x_{s(i+1)}} (EA - T) \frac{1}{2} (W')_{i+1}^4 dx \\
 &+ \frac{1}{2} \sum_{i=1}^n K_i (W_i(x_i, t) - V_i)^2 \\
 &+ \frac{1}{4} \sum_{i=1}^n q_i (W_i(x_i, t) - V_i)^4 \\
 &+ \frac{1}{2} T \sum_{i=0}^n \int_{x_{si}}^{x_{s(i+1)}} (W')_{i+1}^2 dx. \tag{2}
 \end{aligned}$$

Thus, the Lagrangian for the combined system without any nonconservative forces can be expressed as $\mathcal{L} = KE - PE$:

$$\begin{aligned}
 \mathcal{L} &= \sum_{i=0}^n \int_{x_{si}}^{x_{s(i+1)}} m \dot{W}_{i+1}^2 dx \\
 &+ \frac{1}{2} \sum_{i=1}^n M_{ci} \dot{W}_i(x_{si}, t)^2 \\
 &+ \frac{1}{2} \sum_{i=1}^n M_{di} \dot{V}_i(t)^2 \\
 &- \frac{1}{2} \sum_{i=0}^n \int_{x_{si}}^{x_{s(i+1)}} EI(W''_{i+1})^2 dx \\
 &- \frac{1}{2} \sum_{i=0}^n \int_{x_{si}}^{x_{s(i+1)}} (EA - T) \frac{1}{2} (W')_{i+1}^4 dx
 \end{aligned}$$

Fig. 1 Schematic of a transmission cable with attached nonlinear vibration absorbers. (Color figure online)



$$\begin{aligned}
 & -\frac{1}{2} \sum_{i=1}^n K_i (W_i(x_i, t) - V_i)^2 \\
 & -\frac{1}{4} \sum_{i=1}^n q_i (W_i(x_i, t) - V_i)^4 \\
 & -\frac{1}{2} T \sum_{i=0}^n \int_{x_{si}}^{x_{s(i+1)}} (W')_{i+1}^2 dx. \tag{3}
 \end{aligned}$$

After applying Hamilton’s principle to Eq. (3) and including nonconservative forces, the nonlinear governing equations of motion and boundary conditions for the system can be written as:

$$\begin{aligned}
 & m \ddot{W}_i + EI W_i^{iv} - T W_i'' \\
 & = \frac{EA - T}{2L} \sum_{r=0}^n \left[\int_{x_r}^{x_{r+1}} (W'_{r+1})^2 dx \right] W_i'' \\
 & \quad - 2\mu \dot{W}_i + F_{Li}, \tag{4a}
 \end{aligned}$$

$$\begin{aligned}
 & W_1(0, t) = W_1''(0, t) = W_{n+1}(L, t) \\
 & = W_{n+1}''(L, t) = 0, \tag{4b}
 \end{aligned}$$

$$\begin{aligned}
 & \left\{ W_p = W_{p+1} \right\} \Big|_{x=x_{sp}}, \left\{ W'_p = W'_{p+1} \right\} \Big|_{x=x_{sp}}, \left\{ W''_p \right. \\
 & \left. = W''_{p+1} \right\} \Big|_{x=x_{sp}}, \tag{4c}
 \end{aligned}$$

$$\begin{aligned}
 & \left\{ EI (W_p''' - W_{p+1}''') = M_{cp} \ddot{W}_p + K_p (W_p - V_p) \right. \\
 & \left. + q_p (W_p - V_p)^3 + C_{dp} (\dot{W}_p - \dot{V}_p) \right\} \Big|_{x=x_{sp}} \tag{4d}
 \end{aligned}$$

$$\begin{aligned}
 & \left\{ M_{dp} \ddot{V}_p = K_p (W_p - V_p) + q_p (W_p - V_p)^3 \right. \\
 & \left. + C_{dp} (\dot{W}_p - \dot{V}_p) \right\} \Big|_{x=x_{sp}}, \tag{4e}
 \end{aligned}$$

where $i = 1, 2, \dots, n + 1$ and $p = 1, 2, \dots, n$. In Eq. (4a), μ represents the internal damping coefficient,

whereas $F_{Li}(x, t)$ is the fluctuating fluid force across segment i of the cable/conductor. Following Skop and Balasubramanian [1], F_{Li} can be defined in terms of fluctuating lift coefficient $C_{Li}(x, t)$ as:

$$F_{Li} = \frac{\rho_f V_f^2 D C_{Li}}{2}. \tag{5}$$

This model introduces further nonlinearity via C_{Li} . Instead of being constant as in previous works, C_{Li} is governed by the following equation

$$C_{Li}(x, t) = Q_i(x, t) - \frac{2\alpha}{\omega_s} \dot{W}_i(x, t), \tag{6}$$

where α is the stall parameter and ω_s is the vortex shedding frequency. Due to the lock-in condition found in vortex shedding, it can be assumed that $\omega_s \cong \omega_{n,j}$, where $\omega_{n,j}$ is the j^{th} natural frequency for the conductor response. $Q_i(x, t)$ is the wake variable, representing the excitation component of the lift coefficient and is considered to develop from the conductor’s amplitude response. The second term in Eq. (6), also known as a stall term, enforces a self-limiting response for all system parameter values by ensuring that the lift coefficient has a negative slope for large amplitude response. Following Skop and Balasubramanian [1], the wake variable $Q_i(x, t)$ is governed through a nonlinear Van der Pol equation and given by

$$\ddot{Q}_i - \omega_s G (C_{L0}^2 - 4Q_i^2) \dot{Q}_i + \omega_s^2 Q_i = \omega_s F \dot{W}_i, \tag{7}$$

where G and F are parameters depending on the cable-wind interaction and can be determined from experimental data, and C_{L0} is the lift coefficient for a stationary cylinder.

For the ease of analysis, the following nondimensional scales and parameters are introduced in the system:

$$\begin{aligned} \xi &= \frac{x}{L}, \xi_p = \frac{x_{sp}}{L}, w_i = \frac{W_i}{r}, v_p = \frac{V_p}{r}, \tau \\ &= \frac{t}{L^2} \sqrt{\frac{EI}{m}}, s = \sqrt{\frac{TL^2}{2EI}}, \lambda = 1 - 2s^2 \frac{r^2}{L^2}, \\ \bar{\mu} &= \mu \frac{L^4}{EI r}, f_L = \frac{L^4 \rho_f V_f^2 D}{2EI r}, \alpha_{1p} = \frac{M_{cp}}{mL}, \alpha_{2p} \\ &= \frac{M_{dp}}{mL}, k_p = \frac{K_p L^3}{EI}, \gamma_p = \frac{q_p L^3 r^2}{EI}, \\ c_{dp} &= \frac{C_{dp} L^2}{M_{dp}} \sqrt{\frac{m}{EI}}, \bar{\alpha} = \alpha r, \bar{F} = Fr, \bar{\omega}_s \\ &= \omega_s \sqrt{\frac{mL^4}{EI}}. \end{aligned} \tag{8}$$

where r is the radius of gyration of cable. Using the above-mentioned nondimensional scales and parameters, the governing equations of motion can be nondimensionalized as

$$\ddot{w}_i + w_i^v - 2s^2 w_i'' = \frac{\lambda}{2} \sum_{r=0}^n \left[\int_{\xi_r}^{\xi_{r+1}} (w'_{r+1})^2 d\xi \right] w_i'' - 2\bar{\mu} \dot{w}_i + f_L \left(Q_i - \frac{2\bar{\alpha}}{\bar{\omega}_s} \dot{w}_i \right) \tag{9a}$$

$$\ddot{Q}_i - \bar{\omega}_s G (C_{L0}^2 - 4Q_i^2) \dot{Q}_i + \bar{\omega}_s^2 Q_i = \bar{\omega}_s \bar{F} \dot{w}_i \tag{9b}$$

$$\left\{ \alpha_{2p} \ddot{v}_p = k_p (w_p - v_p) + \gamma_p (w_p - v_p)^3 + c_{dp} (\dot{w}_p - \dot{v}_p) \right\} \Big|_{\xi=\xi_p} \tag{9c}$$

$$w_1(0, \tau) = w_1''(0, \tau) = w_{n+1}(1, \tau) = w_{n+1}''(1, \tau) = 0 \tag{9d}$$

$$\left\{ w_p = w_{p+1} \right\} \Big|_{\xi=\xi_p}, \left\{ w'_p = w'_{p+1} \right\} \Big|_{\xi=\xi_p}, \left\{ w''_p = w''_{p+1} \right\} \Big|_{\xi=\xi_p} \tag{9e}$$

$$\left\{ w_p''' - w_{p+1}''' = \alpha_{1p} \ddot{w}_p + k_p (w_p - v_p) + \gamma_p (w_p - v_p)^3 + c_{dp} (\dot{w}_p - \dot{v}_p) \right\} \Big|_{\xi=\xi_p} \tag{9f}$$

Having established the nonlinear governing equations of motion, next a perturbation method is used to obtain an approximate solution of Eq. (9). This method is presented in the following section.

3 Nonlinear analysis using the method of multiple scales

As mentioned earlier, our prime interest in this work is to understand the effect of different system parameters on the nonlinear dynamics of the system, which further requires the exact solution of the system of equations (Eq. (9)). Note that the equations of motion governing the dynamics of the system (Eq. (9)) involve nonlinear cubic terms, and it is difficult to obtain the exact solution for such systems. However, the approximate solution may be obtained using existing perturbation methods. With the same motivation, the method of multiple scales (MMS) is used in particular to obtain the approximate solution of the system. For this purpose, we follow the procedure outlined in [44] and introduce a small dimensionless parameter ϵ ($\epsilon \ll 1$) in the governing equations by defining multiple time scales:

$$T_0 = \tau, \quad T_2 = \epsilon^2 \tau, \tag{10}$$

where T_0 is the fast time scale, T_2 is a slow time scale, and ϵ is a small scaling parameter. Since the type of nonlinearity in the system is cubic in nature, the slow time scale $T_1 = \epsilon \tau$ has not been considered in the system. With the introduction of these time scales, the time derivative operators get perturbed and can be expressed in new time scales as

$$\frac{\delta}{\delta \tau} = D_0 + \epsilon^2 D_2 + O(\epsilon^3) \tag{11a}$$

$$\frac{\delta^2}{\delta \tau^2} = D_0^2 + 2\epsilon^2 D_0 D_2 + O(\epsilon^3) \tag{11b}$$

where $D_n = \frac{\delta}{\delta T_n}$. Following this, the solution of nonlinear governing equations of motion (Eq. (9)) can be expressed as a series in powers of ϵ as

$$w_i(\xi, \tau) = \epsilon y_{i,1}(\xi, T_0, T_2) + \epsilon^3 y_{i,3}(\xi, T_0, T_2) + O(\epsilon^4), \tag{12a}$$

$$Q_i(\xi, \tau) = \epsilon q_{i,1}(\xi, T_0, T_2) + \epsilon^3 q_{i,3}(\xi, T_0, T_2) + O(\epsilon^4), \tag{12b}$$

$$v_p(\tau) = \epsilon v_{p,1}(T_0, T_2) + \epsilon^3 v_{p,3}(T_0, T_2) + O(\epsilon^4). \tag{12c}$$

As we are considering the case of primary resonance, i.e., $\omega_s \approx \omega_y$, the following parameters are rescaled to ensure that the system is weakly nonlinear and that the effects of damping and forcing appear at the same order ϵ

$$\begin{aligned}
 f_L &= \epsilon^2 f_L^*, \bar{\mu} = \epsilon^2 \bar{\mu}^*, c_{dp} = \epsilon^2 c_{dp}^*, F \\
 &= \epsilon^2 F^*, GC_{L0}^2 = \epsilon^2 G (C_{L0}^*)^2.
 \end{aligned}
 \tag{13}$$

Through introducing Eqs. (11)–(13) into Eq. (9) and collecting different orders of ϵ to get $\mathcal{O}(\epsilon^1)$:

$$D_0^2 y_{i,1} + y_{i,1}^{iv} - 2s^2 y_{i,1}'' = 0, \tag{14a}$$

$$D_0^2 q_{i,1} + \bar{\omega}_s^2 q_{i,1} = 0, \tag{14b}$$

$$\alpha_{2p} D_0^2 v_{p,1} - k_p (y_{p,1} - v_{p,1}) \Big|_{\xi=\xi_p} = 0, \tag{14c}$$

$$\begin{aligned}
 y_{1,1}(0, \tau) &= y_{1,1}''(0, \tau) = y_{(n+1),1}(1, \tau) \\
 &= y_{(n+1),1}''(1, \tau) = 0,
 \end{aligned}
 \tag{14d}$$

$$\begin{aligned}
 \{y_{p,1} = y_{(p+1),1}\} \Big|_{\xi=\xi_p}, \{y'_{p,1} \\
 = y'_{(p+1),1}\} \Big|_{\xi=\xi_p}, \{y''_{p,1} = y''_{(p+1),1}\} \Big|_{\xi=\xi_p},
 \end{aligned}
 \tag{14e}$$

$$\begin{aligned}
 \{y'''_{p,1} - y'''_{(p+1),1} = \alpha_{1p} D_0^2 y_{p,1} \\
 + k_p (y_{p,1} - v_{p,1})\} \Big|_{\xi=\xi_p},
 \end{aligned}
 \tag{14f}$$

$\mathcal{O}(\epsilon^3)$:

$$\begin{aligned}
 D_0^2 y_{i,3} + y_{i,3}^{iv} - 2s^2 y_{i,3}'' \\
 = \frac{\lambda}{2} \sum_{r=0}^n \left[\int_{\xi_r}^{\xi_{r+1}} (y')^2_{(r+1),1} d\xi \right] y_{i,1}'' \\
 - 2D_0 D_2 y_{i,1} - 2\bar{\mu}^* D_0 y_{i,1} \\
 + f_L^* \left(q_{i,1} - \frac{2\bar{\alpha} D_0 y_{i,1}}{\bar{\omega}_s} \right),
 \end{aligned}
 \tag{15a}$$

$$\begin{aligned}
 D_0^2 q_{i,3} + q_{i,3} \bar{\omega}_s^2 = GC_{L0}^*{}^2 D_0 q_{i,1} \bar{\omega}_s \\
 - 4G D_0 q_{i,1} q_{i,1}^2 \bar{\omega}_s - 2D_0 D_2 q_{i,1} \\
 + F^* D_0 w_{i,1} \bar{\omega}_s,
 \end{aligned}
 \tag{15b}$$

$$\begin{aligned}
 \left\{ \alpha_{2p} D_0^2 v_{p,3} - k_p (y_{p,3} - v_{p,3}) = -\alpha_{2p} 2D_0 D_2 v_{p,1} \right. \\
 \left. + \gamma_p (y_{p,1} - v_{p,1})^3 + c_{dp}^* D_0 (y_{p,1} - v_{p,1}) \right\} \Big|_{\xi=\xi_p}
 \end{aligned}
 \tag{15c}$$

$$\begin{aligned}
 y_{1,3}(0, \tau) &= y_{1,3}''(0, \tau) = y_{(n+1),3}(1, \tau) \\
 &= y_{(n+1),3}''(1, \tau) = 0,
 \end{aligned}
 \tag{15d}$$

$$\begin{aligned}
 \{y_{p,3} = y_{(p+1),3}\} \Big|_{\xi=\xi_p}, \{y'_{p,3} = y'_{(p+1),3}\} \Big|_{\xi=\xi_p}, \\
 \{y''_{p,3} = y''_{(p+1),3}\} \Big|_{\xi=\xi_p},
 \end{aligned}
 \tag{15e}$$

$$\begin{aligned}
 \left\{ y'''_{p,3} - y'''_{(p+1),3} = k_p (y_{p,3} - v_{p,3}) \right. \\
 + \gamma_p (y_{p,1} - v_{p,1})^3 + c_{dp}^* D_0 (y_{p,1} - v_{p,1}) \\
 \left. + \alpha_{1p} D_0^2 y_{p,3} + \alpha_{1p} 2D_0 D_2 y_{p,1} \right\} \Big|_{\xi=\xi_p},
 \end{aligned}
 \tag{15f}$$

Note that the equations at the order of $\mathcal{O}(\epsilon^1)$ (Eq. (14)) are linear coupled partial differential equations. Also, the solution of the $\mathcal{O}(\epsilon^1)$ appears on right side as forcing terms for the equations corresponding to $\mathcal{O}(\epsilon^3)$ (Eq. (15)). Therefore, it is required to perform the linear analysis of the system, which is presented in the subsequent section.

3.1 Linear analysis

As mentioned earlier, equations corresponding to $\mathcal{O}(\epsilon^1)$ are coupled linear partial differential equations. Therefore, the system only consists of linear harmonic vibrations and the solutions of $y_{i,1}$ and $v_{p,1}$ can be expressed as [45]:

$$y_{i,1} = \left[A_1(T_2) e^{j\omega_y T_0} + c.c. \right] Y_i(\xi), \tag{16}$$

$$v_{p,1} = V_{1,p}(T_2) e^{j\omega_y T_0} + c.c., \tag{17}$$

where *c.c.* denotes the complex conjugate of the preceding temporal term and $Y_i(\xi)$ is the spatial solution or mode shape for the i^{th} segment of the cable. From the experimental work of Ramberg and Griffin [46], it was shown that the wake term of a vortex-induced excitation shares the normal modes of the conductor response. Thus, the mode shape $Y_i(\xi)$ is identical for both $y_{i,1}$ and $q_{i,1}$ [46,47] and hence, the solution for $q_{i,1}$ can be written as

$$q_{i,1} = \left[\tilde{Q}_1(T_2) e^{j\bar{\omega}_s T_0} + c.c. \right] Y_i(\xi), \tag{18}$$

Substitution of the assumed form of the solutions for $y_{i,1}$, $v_{p,1}$ and $q_{i,1}$ into Eq. (14) leads to

$$Y_i^{iv} - 2s^2 Y_i'' - \omega_y^2 Y_i = 0, \tag{19a}$$

$$-\omega_s^2 \tilde{Q}_1 + \omega_s^2 \tilde{Q}_1 = 0, \tag{19b}$$

$$-\omega_y^2 \alpha_{2p} V_{1,p} - k_p (A_1 Y_i(\xi_p) - V_{1,p}) = 0, \tag{19c}$$

$$Y_1(0) = Y_1''(0) = Y_{(n+1)}(1) = Y_{(n+1)}''(1) = 0, \tag{19d}$$

$$\begin{aligned}
 \{Y_p = Y_{(p+1)}\} \Big|_{\xi=\xi_p}, \{Y'_p = Y'_{(p+1)}\} \Big|_{\xi=\xi_p}, \{Y''_p \\
 = Y''_{(p+1)}\} \Big|_{\xi=\xi_p},
 \end{aligned}
 \tag{19e}$$

$$\begin{aligned}
 \left\{ Y'''_p - Y'''_{(p+1)} = -\omega_y^2 \alpha_{1p} Y_p \right. \\
 \left. + k_p \left(Y_p - \frac{V_{1,p}}{A_1} \right) \right\} \Big|_{\xi=\xi_p}.
 \end{aligned}
 \tag{19f}$$

Note that Eq. (19b) does not provide any additional information for the linear analysis, as $q_{i,1}$ and $y_{i,1}$ share the same mode shapes. Also, from Eq. (19c) it can be

noticed that $V_{1,p}$ and A_1 are related through the following expression

$$V_{1,p} = \left(\frac{k_p}{k_p - \alpha_{2p}\omega_y^2} \right) Y_p(\xi_p) A_1 = \Psi_p Y_p(\xi_p) A_1 \tag{20}$$

with $\Psi_p = \frac{k_p}{k_p - \alpha_{2p}\omega_y^2}$. The mode shape Y_i for each segment of cable can be obtained by solving Eq. (19a) and is given by

$$Y_i = C_{1,i} \sin \alpha \xi + C_{2,i} \cos \alpha \xi + C_{3,i} \sinh \beta \xi + C_{4,i} \cosh \beta \xi \tag{21}$$

where α and β are functions of the beam's natural frequency ω_y and s , and are given by

$$\alpha = \sqrt{-s^2 + \sqrt{s^4 + \omega_y^4}}, \quad \beta = \sqrt{s^2 + \sqrt{s^4 + \omega_y^4}}. \tag{22}$$

Whereas $C_{k,i}$, $k = 1, 2, 3, 4$ are arbitrary coefficients. The natural frequencies of the system, i.e., ω_y for different modes, and accordingly, the arbitrary coefficients can be determined by utilizing boundary conditions for the nontrivial solutions of the system. We emphasize that due to the complex boundary conditions, it is not possible to obtain closed form expression for the natural frequency for different modes. Therefore, numerical methods are used to compute the natural frequencies and corresponding arbitrary coefficients. Having established the linear solution of the system, the nonlinear analysis using the equations corresponding to $\mathcal{O}(\epsilon^3)$ is presented next.

3.2 Nonlinear analysis

Since linear analysis does not provide any information about the nonlinear response of the system, we proceed to equations corresponding to $\mathcal{O}(\epsilon^3)$. To have a finite solution of the system described by Eq. (15), the solvability conditions must be determined and satisfied, i.e., the coefficients corresponding to secular terms must vanish. To achieve this, the solutions of $y_{i,3}$, $v_{p,3}$ are assumed as

$$y_{i,3} = \phi_i(\xi, T_2) e^{j\omega_y T_0} + c.c. + y_i^*(\xi, T_0, T_2), \tag{23a}$$

$$v_{p,3} = V_{2,p}(T_2) e^{j\omega_y T_0} + c.c. + v_p^*(T_0, T_2), \tag{23b}$$

where y_i^* and v_p^* are the unique expressions that do not produce any secular terms in Eq. (15) and hence are not

reported here (for more details about these terms readers are referred to [48]). As mentioned earlier, in the current work, we are considering the case of primary resonance only that accompanies lock-in phenomena. In the lock-in phenomena, the vortex shedding frequency is detuned from one of the natural frequencies of the system by a small parameter and hence, can be related to the natural frequency of the system by the following expression

$$\omega_s = \omega_y + \epsilon^2 \sigma, \tag{24}$$

where ϵ is the same small parameter as above and σ is the detuning parameter.

Substitution of Eqs. (16)–(18), (20), (23), (24) into Eq. (15) and removal of secular terms leads to

$$\begin{aligned} &\phi_i^{iv} - \omega_y^2 \phi_i - 2s^2 \phi_i'' \\ &= \frac{3}{2} \lambda A_1 \bar{A}_1^2 \sum_{r=0}^n \left[\int_{\xi_r}^{\xi_{r+1}} Y_{(r+1)}'^2 d\xi \right] Y_{i,1}'' \\ &\quad - 2j\omega_y (D_2 A_1 + \bar{\mu}^* A_1) Y_i \\ &\quad + f_L^* Y_i \left(Q_1 e^{j\sigma T_2} - \frac{2j\bar{\alpha}\omega_y}{\omega_s} A_1 \right) \end{aligned} \tag{25a}$$

$$\begin{aligned} &4j\omega_s^2 G \bar{Q}_1 \bar{Q}_1 Y_i^3 \\ &\quad - j\omega_s^2 C_{L0}^2 G \bar{Q}_1 Y_i - j\omega_s F^* \omega_y A_1 Y_i e^{-j\sigma T_2} \\ &\quad + 2j\omega_s D_2 \bar{Q}_1 = 0 \end{aligned} \tag{25b}$$

$$\begin{aligned} &- \alpha_{2p} \omega_s^2 V_{2,p} + 2j\omega_y \alpha_{2p} \Psi_p Y_p(\xi_p) D_2 A_1 \\ &= \left\{ k_p (\phi_p - V_{2,p}) - 3\gamma_p \Psi_{1,p} A_1^2 \bar{A}_1 Y_p^3 \right. \\ &\quad \left. + j\omega_y c_{dp}^* Y_p A_1 (1 - \Psi_p) \right\} \Big|_{\xi=\xi_p} \end{aligned} \tag{25c}$$

$$\begin{aligned} \phi_1(0, T_2) &= \phi_1''(0, T_2) \\ &= \phi_{i+1}(0, T_2) = \phi_{i+1}''(0, T_2) = 0 \end{aligned} \tag{25d}$$

$$\begin{aligned} &\left\{ \phi_p = \phi_{p+1} \right\} \Big|_{\xi=\xi_p}, \left\{ \phi_p' \right. \\ &= \left. \phi_{p+1}' \right\} \Big|_{\xi=\xi_p}, \left\{ \phi_p'' \right. \\ &= \left. \phi_{p+1}'' \right\} \Big|_{\xi=\xi_p} \end{aligned} \tag{25e}$$

$$\begin{aligned} &\left\{ \phi_p''' - \phi_{p+1}''' = k_p (\phi_p - V_{2,p}) - 3\gamma_p \Psi_{1,p} A_1^2 \bar{A}_1 Y_p^3 \right. \\ &\quad \left. + j\omega_y c_{dp}^* Y_p A_1 (1 - \Psi_p) + \alpha_{1p} (-\omega_y^2 \phi_p \right. \\ &\quad \left. + 2j\omega_y D_2 A_1 Y_p) \right\} \Big|_{\xi=\xi_p} \end{aligned} \tag{25f}$$

with $\Psi_{1,p} = 1 - \Psi_p^3 + 3\Psi_p^2 - 3\Psi_p$. Further, Eq. (25c) can be rearranged and $V_{2,p}$ can be expressed in terms of other variables as

$$V_{2,p} = \frac{k_p \phi_p(\xi_p, T_2) - 3\gamma_p Y_p(\xi_p)^3 \Psi_{1,p} A_1^2 \bar{A}_1 - 2j\alpha_{2p} \Psi_p Y_p(\xi_p) (D_2 A_1) \omega_y + j c_{dp}^* Y_p(\xi_p) \omega_y (1 - \Psi_p) A_1}{k_p - \alpha_{2p} \omega_y^2}. \tag{26}$$

Using the above expression, Eq. (25f) can be rewritten as

$$\begin{aligned} &\phi_p'''(\xi_p, T_2) - \phi_{p+1}'''(\xi_p, T_2) \\ &= -3\gamma_p Y_p(\xi_p)^3 \Psi_{1,p} A_1^2 \bar{A}_1 + 3\Psi_{2,p} k_p A_1^2 \bar{A}_1 \\ &\quad + j D_2 A_1 k_p \omega_y \Psi_{3,p} + j k_p \omega_y A_1 (\Psi_p - 1) \Psi_{4,p} \tag{27} \\ &\quad - j \omega_y (c_{dp}^* \Psi_p A_1 - c_{dp}^* A_1 - 2\alpha_{1p} D_2 A_1) Y_p(\xi_p) \\ &\quad - (\alpha_{1p} \omega_y^2 + k_p \Psi_p - k_p) \phi_p(\xi_p, T_2) \end{aligned}$$

With further algebraic manipulation, Eq. (25) can be simplified to a pair of equations in terms of the magnitudes A_1 and \bar{Q}_1 . These equations are the solvability conditions and are given by

$$\begin{aligned} &\sum_{p=1}^n \left[-3\Psi_{1,p} \gamma_p A_1^2 \bar{A}_1 Y_p(\xi_p)^4 \right. \\ &\quad + \left. \left[j \omega_y (-c_{dp}^* \Psi_p + c_{dp}^*) A_1 + 2j \omega_y \alpha_{1p} D_2 A_1 \right] Y_p(\xi_p)^2 \right. \\ &\quad + \left. \left[(3\Psi_{2,p} k_p A_1^2 \bar{A}_1 + j k_p \omega_y \Psi_{4,p} (\Psi_p - 1) A_1 \right. \right. \\ &\quad + \left. \left. j k_p \omega_y \Psi_{3,p} D_2 A_1 \right] Y_p(\xi_p) \right] \\ &\quad - \frac{3}{2} \lambda b_2 b_3 A_1^2 \bar{A}_1 + \frac{2j b_1 \omega_y}{\omega_s} (f_L^* \bar{\alpha} + \bar{\mu}^* \omega_s) A_1 \\ &\quad + 2j b_1 \omega_y D_2 A_1 - e^{j\sigma T_2} f_L^* \bar{Q}_1 b_1 \\ &= 0, \tag{28} \end{aligned}$$

$$\begin{aligned} &2e^{j\sigma T_2} D_2 Q_1 - e^{j\sigma T_2} b_1 \omega_s G C_{L0}^* Q_1 \\ &\quad - F^* \omega_y b_1 A_1 + 4G \omega_s b_{12} e^{j\sigma T_2} Q_1^2 \bar{Q}_1 \\ &= 0, \tag{29} \end{aligned}$$

with

$$\begin{aligned} \Psi_{2,p} &= \frac{\gamma_p \Psi_{1,p} Y_p(\xi_p)^3}{k_p - \alpha_{2p} \omega_y^2}, \Psi_{3,p} \\ &= \frac{2\alpha_{2p} \Psi_{1,p} Y_p(\xi_p)}{k_p - \alpha_{2p} \omega_y^2}, \Psi_{4,p} = \frac{c_{dp}^* Y_p(\xi_p)}{k_p - \alpha_{2p} \omega_y^2} \tag{30} \end{aligned}$$

$$\begin{aligned} b_1 &= \sum_{p=1}^{n+1} \int_{\xi_{p-1}}^{\xi_p} Y_p^2 d\xi, \quad b_{12} = \sum_{p=1}^{n+1} \int_{\xi_{p-1}}^{\xi_p} Y_p^4 d\xi, \quad b_2 \\ &= \sum_{p=1}^{n+1} \int_{\xi_{p-1}}^{\xi_p} \left(\frac{d}{d\xi} Y_p \right)^2 d\xi, \quad b_3 \end{aligned}$$

$$= \sum_{p=1}^{n+1} \int_{\xi_{p-1}}^{\xi_p} Y_p \left(\frac{d}{d\xi} Y_p \right)^2 d\xi \tag{31}$$

Next, we switch to polar coordinates by substituting

$$\begin{aligned} A_1(T_2) &= \frac{a_y(T_2) e^{i\theta_y(T_2)}}{2} \\ \text{and } \bar{A}_1(T_2) &= \frac{a_y(T_2) e^{-i\theta_y(T_2)}}{2}, \\ \tilde{Q}_1(T_2) &= \frac{1}{2} q_y(T_2) e^{j\theta_q(T_2)} \\ \text{and } \bar{\tilde{Q}}_1(T_2) &= \frac{1}{2} q_y(T_2) e^{-j\theta_q(T_2)} \quad \text{and} \tag{32} \end{aligned}$$

into Eq. (31) and separate real and imaginary parts. Upon separating real and imaginary parts, we get four equations that can be solved for $D_2 a_y$, $D_2 \theta_y$, $D_2 q_y$ and $D_2 \theta_q$ as

$$\begin{aligned} D_2 a_y &= \frac{\sum_{p=1}^n \left[a_y c_{dp}^* (\Psi_p - 1) Y_p(\xi_p)^2 + a_y k_p \Psi_{4,p} (1 - \Psi_p) Y_p(\xi_p) \right]}{\sum_{p=1}^n \left[k_p Y_p(\xi_p) \Psi_{3,p} + 2Y_p(\xi_p)^2 \alpha_{1p} \right] + 2b_1} \\ &\quad - \frac{2\omega_y a_y f_L^* \bar{\alpha} b_1 - f_L^* q_y b_1 \omega_s \sin(\Gamma) + 2\omega_y a_y \bar{\mu}^* b_1 \omega_s}{\sum_{p=1}^n \left[\omega_s \omega_y k_p Y_p(\xi_p) \Psi_{3,p} + 2\omega_s \omega_y Y_p(\xi_p)^2 \alpha_{1p} \right] + 2\omega_y \omega_s b_1}, \tag{33a} \end{aligned}$$

$$\begin{aligned} D_2 \theta_y &= \frac{\sum_{p=1}^n (6a_y^3 k_p Y_p(\xi_p) \Psi_{2,p} - 6a_y^3 \gamma_p Y_p(\xi_p)^4 \Psi_{1,p})}{\sum_{p=1}^n a_y \omega_y \left[16b_1 + 8k_p Y_p(\xi_p) \Psi_{3,p} + 16Y_p(\xi_p)^2 \alpha_{1p} \right]} \\ &\quad + \frac{-8f_L^* q_y b_1 \cos(\Gamma) - 3a_y^3 \lambda b_2 b_3}{\sum_{p=1}^n a_y \omega_y \left[16b_1 + 8k_p Y_p(\xi_p) \Psi_{3,p} + 16Y_p(\xi_p)^2 \alpha_{1p} \right]}, \tag{33b} \end{aligned}$$

$$\begin{aligned} D_2 q_y &= \frac{1}{2b_1} a_y F^* \omega_y b_1 \cos(\Gamma) + \omega_s G C_{L0}^* q_y b_1 \\ &\quad - q_y^3 G \omega_s b_{12}, \tag{33c} \end{aligned}$$

$$D_2 \theta_q = -\frac{1}{2q_y} a_y F^* \omega_y \sin(\Gamma). \tag{33d}$$

In the above slow-flow equations, the phase difference, Γ , is defined as $\Gamma = \sigma T_2 + \theta_q - \theta_y$. Note that Eq. (33) provides the dynamics of the system in the slow time scale T_2 . Therefore, the equilibrium solution of the system at T_2 is equivalent to the steady-state amplitudes of the full-order system, i.e., Eq. (9).

The steady-state amplitudes are solved by setting the time derivatives of amplitude and phase to zero, i.e., $D_2 a_y = D_2 q_y = D_2 \Gamma = 0$. This step gives us 3 algebraic equations in terms of a_y and q_y with trigonometric terms of an argument of phase difference Γ . Eliminating the phase difference Γ by using trigonometric identities, two algebraic equations governing the unknown steady-state amplitudes a_y^* , q_y^* for the given system parameters are obtained as

$$G_1(a_y^*, q_y^*) = 0 \quad \text{and} \quad G_2(a_y^*, q_y^*) = 0. \tag{34}$$

For the sake of brevity, the expressions for G_1 and G_2 have been put in Appendix-A. Having established the slow-flow equations governing the steady-state response, a detailed discussion on these slow flow equations and verification of our analytical approach with numerical simulation are presented in the next section.

4 Results and discussion

In this section, a detailed analysis of the VIV of a cable/conductor with an installed nonlinear vibration absorber in the form of a Stockbridge damper is presented. The first part of the analysis deals with the validation of the derived analytical solution of the system using MMS (Eq. (33)) and determines the value of ϵ (dependent on the system parameters) that validates our assumption of a weakly nonlinear system. One of the ways to validate our analytical solutions is the comparison of the analytical solutions, obtained using MMS, with the numerical solution of the system given by Eq. (9). However, it can be noted that the original system defined by Eq. (9) is an infinite-dimensional system due to appearance of spatial derivatives and hence, limits the application of numerical solvers to the system. To overcome this challenge, the infinite dimensional partial-differential system is converted to a finite-dimensional system of ordinary differential equation (odes) using Galerkin projection. This is presented in the subsequent section.

4.1 Validation of analytical results From MMS

To numerically analyze the nonlinear dynamical problem defined by Eq. (9) and eventually use these simulations to validate analytical results, we first cast these equations (Eq. (9)) in state-space (first-order) form. By

utilizing the orthonormality properties of linear mode shapes, Eq. (9) are projected onto the system of eigenfunctions by letting

$$w_i(\xi, \tau) = Y_i(\xi)y(\tau), \tag{35}$$

$$\text{and} \quad Q_i(\xi, \tau) = \hat{Q}_i(\xi)q(\tau),$$

with $Y_i(\xi)$ and $Q_i(\xi)$ being functions of spatial coordinate ξ and satisfying linear boundary conditions. As mentioned earlier, $Q_i(\xi, \tau)$ and $w_i(\xi, \tau)$ share the same mode shapes, which further implies $\hat{Q}_i(\xi) = Y_i(\xi)$. Since in our linear analysis, an exact linear mode shape with linear boundary conditions, i.e., $\gamma_p = c_{dp} = 0$, is obtained, the Galerkin projection of Eq. (9) cannot be performed using the mode shape defined by Eq. (21) due to the appearance of nonlinear and damping terms, i.e., γ_p and c_{dp} in boundary conditions. To resolve this, we include γ_p and c_{dp} in the governing equations of motion using Dirac delta function and rewrite Eq. (9) to get

$$\ddot{w}_i + w_i^{iv} - 2s^2 w_i''$$

$$= \frac{\lambda}{2} \sum_{r=0}^n \left[\int_{\xi_r}^{\xi_{r+1}} (w'_{r+1})^2 d\xi \right] w_i''$$

$$- 2\mu \dot{w}_i + f_L \left(Q_i - \frac{2\bar{\alpha}}{\bar{\omega}_s} \dot{w}_i \right)$$

$$- \delta(\xi - \xi_i) (\gamma_i (v_i - w_i)^3$$

$$+ c_{di} (\dot{v}_i - \dot{w}_i)) \quad (i = 1, 2, \dots, n), \tag{36a}$$

$$\ddot{w}_{n+1} + w_{n+1}^{iv} - 2s^2 w_{n+1}''$$

$$= \frac{\lambda}{2} \sum_{r=0}^n \left[\int_{\xi_r}^{\xi_{r+1}} (w'_{r+1})^2 d\xi \right] w_{n+1}''$$

$$- 2\mu \dot{w}_{n+1} + f_L \left(Q_{n+1} - \frac{2\bar{\alpha}}{\bar{\omega}_s} \dot{w}_{n+1} \right), \tag{36b}$$

$$\ddot{Q}_i - \bar{\omega}_s G (C_{L0}^2 - 4Q_i^2) \dot{Q}_i + \bar{\omega}_s^2 Q_i$$

$$= \bar{\omega}_s \bar{F} \dot{w}_i \quad (i = 1, 2, \dots, n + 1), \tag{36c}$$

$$\left\{ \alpha_{2p} \ddot{v}_p = k_p (w_p - v_p) + \gamma_p (w_p - v_p)^3 \right.$$

$$\left. + c_{dp} (\dot{w}_p - \dot{v}_p) \right\} \Big|_{\xi=\xi_p}, \tag{36d}$$

$$w_1(0, \tau) = w_1''(0, \tau)$$

$$= w_{n+1}(1, \tau) = w_{n+1}''(1, \tau) = 0, \tag{36e}$$

$$\left\{ w_p = w_{p+1} \right\} \Big|_{\xi=\xi_p}, \left\{ w'_p = w'_{p+1} \right\} \Big|_{\xi=\xi_p}, \left\{ w''_p \right.$$

$$\left. = w''_{p+1} \right\} \Big|_{\xi=\xi_p}, \tag{36f}$$

$$\left\{ w'''_p - w'''_{p+1} = \alpha_{1p} \ddot{w}_p + k_p (w_p - v_p) \right\} \Big|_{\xi=\xi_p}, \tag{36g}$$

Since for the modified governing equations of motion (Eq. (36)), the mode shape defined by Eq. (21) satisfies all the boundary conditions (Eqs. (36e)-(36g)), the

Galerkin projection of Eq. (36) can be performed using the mode shape defined by Eq. (21) to get

$$\begin{aligned}
 & b_1 \ddot{y}(\tau) + \left(2b_1 \mu + \frac{2b_1 f_L \alpha}{\bar{\omega}_s} \right) \dot{y}(\tau) - 2b_3 s^2 y(\tau) \\
 & - \frac{\lambda}{2} b_3 b_2 y(\tau)^3 + b_4 y(\tau) - b_1 f_L q(\tau) \\
 & + \frac{1}{2} \sum_{p=1}^n [\gamma_p Y_p(\xi_p) (y(\tau) Y_p(\xi_p) \\
 & - v_p(\tau))^3 + c_{dp} Y_p(\xi_p) (\dot{y}(\tau) Y_p(\xi_p) \\
 & - \dot{v}_p(\tau))] = 0, \tag{37a}
 \end{aligned}$$

$$\begin{aligned}
 & b_1 \ddot{q}(\tau) - \omega_s G (b_1 C_{L0}^2 - 4q^2(\tau) b_{12}) \dot{q}_1 \\
 & + b_1 \omega_s^2 q(\tau) - b_1 \dot{y}(\tau) \omega_s \bar{F} = 0, \tag{37b}
 \end{aligned}$$

$$\begin{aligned}
 & \alpha_{2p} \ddot{v}_p = k_p (Y_p(\xi_p) y(\tau) - v_p(\tau)) \\
 & + \gamma_p (Y_p(\xi_p) y(\tau) - v_p(\tau))^3 \\
 & + c_{dp} (Y_p(\xi_p) \dot{y}(\tau) - \dot{v}_p(\tau)) \quad (p = 1, 2, \dots, n). \tag{37c}
 \end{aligned}$$

with b_1, b_2, b_3, b_{12} defined in Eq. (31). Equation (37) defines the dynamics of the reduced order system. Further, for the sake of simplicity, these equations can be written as first-order ODES and given by

$$\dot{z}_1 = z_2, \tag{38a}$$

$$\begin{aligned}
 \dot{z}_2 = & -\frac{1}{b_1} \left(\left(2b_1 \mu + \frac{2b_1 f_L \alpha}{\bar{\omega}_s} \right) z_2 \right. \\
 & - 2b_3 s^2 z_1 - \frac{\lambda}{2} b_3 b_2 z_1^3 + b_4 z_1 - b_1 f_L z_3 \\
 & \left. + \frac{1}{2} \sum_{p=1}^n [\gamma_p Y_p(\xi_p) (z_1 Y_p(\xi_p) \right. \\
 & - z_{(2p+3)}(\tau))^3 + c_{dp} Y_p(\xi_p) (z_2 Y_p(\xi_p) \\
 & \left. - z_{(2p+4)})] \right), \tag{38b}
 \end{aligned}$$

$$\dot{z}_3 = z_4, \tag{38c}$$

$$\begin{aligned}
 \dot{z}_4 = & -\frac{1}{b_1} (-\omega_s G (b_1 C_{L0}^2 - 4q^2(\tau) b_{12}) \dot{q}_1 \\
 & + b_1 \omega_s^2 q(\tau) - b_1 \dot{y}(\tau) \omega_s \bar{F}), \tag{38d}
 \end{aligned}$$

$$\dot{z}_{2p+3} = z_{2p+4}, \quad (p = 1, 2, \dots, n) \tag{38e}$$

$$\begin{aligned}
 \dot{z}_{2p+4} = & \frac{1}{\alpha_{2p}} (k_p (Y_p(\xi_p) z_1 - z_{2p+3}) + \gamma_p (Y_p(\xi_p) z_1 \\
 & - z_{2p+3})^3 + c_{dp} (Y_p(\xi_p) z_2 - z_{2p+4})) \quad (p = 1, 2, \dots, n). \tag{38f}
 \end{aligned}$$

For the numerical simulations, MATLAB routine ‘ode45’ is used with strict values of relative and absolute tolerance ($1e^{-10}$). Also, the initial conditions for

the numerical simulation are chosen corresponding to the steady-states. The comparisons between the numerical simulation of the system given by Eq. (38) and analytical results from MMS for the lock-in phenomenon near the first mode, i.e., $\omega_y = \omega_1$ and two vibration absorbers are shown in Figs. 2, 3, 4 for different values of ϵ and $\sigma = 0.1$. From Figs. 3 and 4, it can be observed that there is no significant difference between $\epsilon = 0.01$ and $\epsilon = 0.001$, and an excellent agreement holds between the numerical simulations and analytical for both values of ϵ . Therefore, without any loss of generality, we have chosen the value of $\epsilon = 0.01$ in the remaining analysis.

Before proceeding further, we compare the time-response of the system with and without nonlinearity in vibration absorbers for different values of detuning parameter. The results are shown in Fig. 5. Note that this step also elucidates the performance of the nonlinear absorber over the linear absorber.

From Fig. 5, we can observe that around the primary resonance, i.e., $\omega_y = \omega_s$ the maximum amplitude of the system with nonlinear absorber (Solid Blue curve) is smaller than that of the system with linear absorber (Dashed Red curve). This observation further motivates us to perform a parametric analysis on the system with nonlinear absorber to identify key design parameters which can enhance the performance of a vibration absorber which is presented next.

4.2 Effect of parameters on system dynamics

In this section, we present the effect of different system parameters on the dynamics of the system to identify the key design parameters. However, before proceeding further, the comparison of the system dynamics with lift force modeled as a wake oscillator against the system with lift force modeled as a sinusoidal force [21] is presented. This step also acts as a motivation to perform the parametric analysis of the system. Figure 6 shows the variation of the steady-state response of the wake variable q_y with the detuning parameter σ . From Fig. 6, it can be observed that unlike a traditional sinusoidal model for the lift force, where excitation amplitude does not depend on the frequency and time, the wake variable q_y displays interesting dynamics near the 0 value of the detuning parameter. Note that $\sigma = 0$ signifies the complete resonance phenomenon between the primary system, i.e., cable with vibration

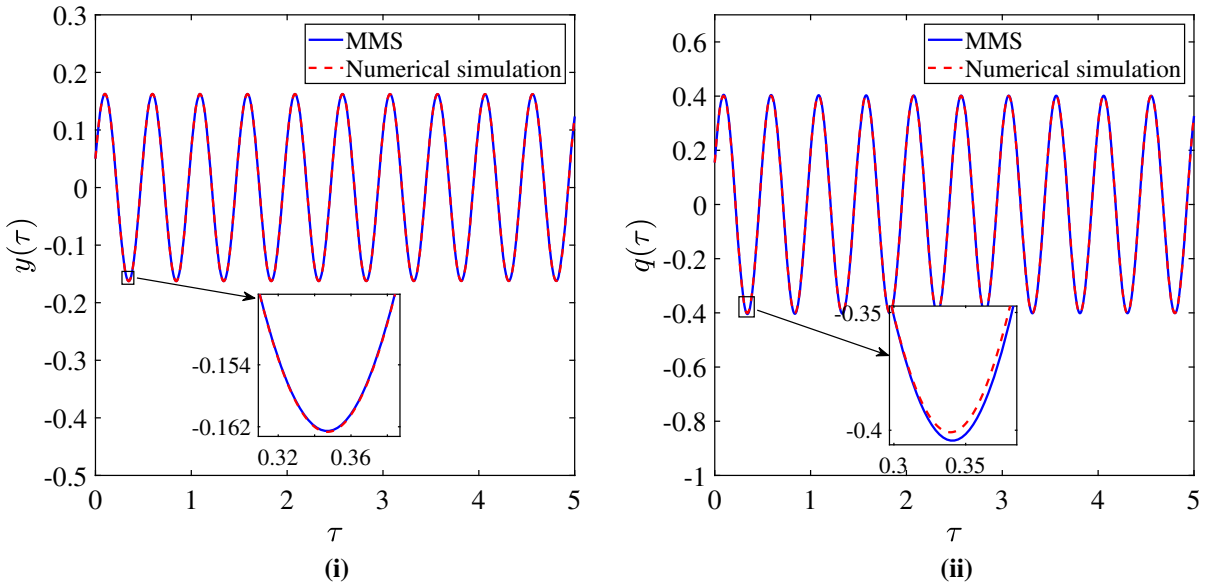


Fig. 2 Comparison of time response of the system obtained from the method of multiple scales (solid line) and numerical simulation (dashed line) for (i) the response of cable, and (ii) the response of wind-excitation with $\epsilon = 0.1$. The other system parameters are $\xi_1 = 0.1, \xi_2 = 0.9, \alpha_{11} = \alpha_{12} =$

$.01, \alpha_{21} = \alpha_{22} = .2, k_{11} = k_{12} = 2\pi^4, s = 2, f_L = 0.2, \alpha = 0.01, c_{d1} = c_{d2} = 0, \gamma_1 = \gamma_2 = 0, C_{L0} = 0.28, F = 1.2534e^{-2}, G = 0.3763, \lambda = 0.9988, \bar{\mu} = 0.002,$ and $\sigma = -0.1$. (Color figure online)

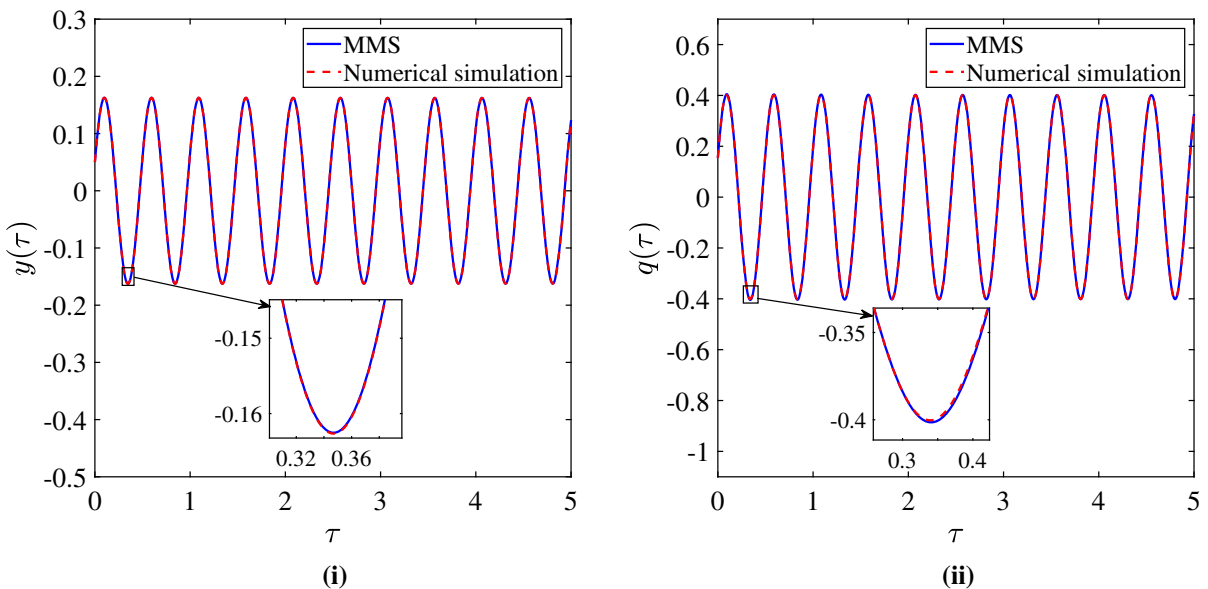


Fig. 3 Comparison of time response of the system obtained from the method of multiple scales (solid line) and numerical simulation (dashed line) for (i) the response of cable, and (ii) the response of wind-excitation with $\epsilon = 0.01$. The other system parameters are $\xi_1 = 0.1, \xi_2 = 0.9, \alpha_{11} = \alpha_{12} =$

$.01, \alpha_{21} = \alpha_{22} = .2, k_{11} = k_{12} = 2\pi^4, s = 2, f_L = 0.2, \alpha = 0.01, c_{d1} = c_{d2} = 0, \gamma_1 = \gamma_2 = 0, C_{L0} = 0.28, F = 1.2534e^{-2}, G = 0.3763, \lambda = 0.9988, \bar{\mu} = 0.002,$ and $\sigma = -0.1$. (Color figure online)

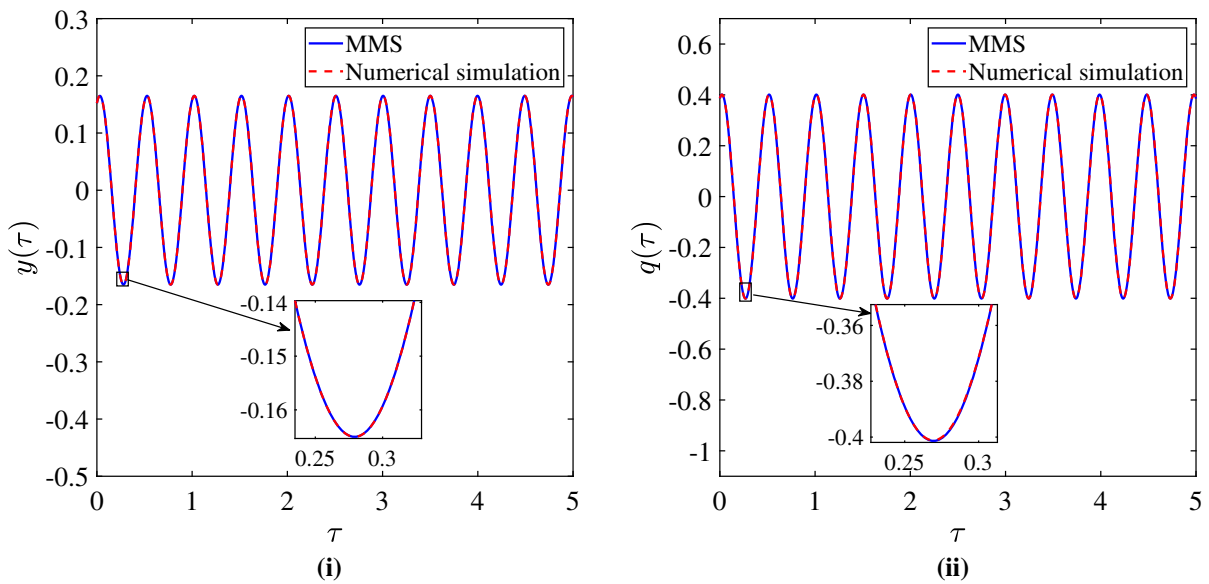


Fig. 4 Comparison of time response of the system obtained from the method of multiple scales (solid line) and numerical simulation (dashed line) for (i) the response of cable, and (ii) the response of wind-excitation with $\epsilon = 0.001$. The other system parameters are $\xi_1 = 0.1$, $\xi_2 = 0.9$, $\alpha_{11} = \alpha_{12} =$

$.01$, $\alpha_{21} = \alpha_{22} = .2$, $k_{11} = k_{12} = 2\pi^4$, $s = 2$, $f_L = 0.2$, $\alpha = 0.01$, $c_{d1} = c_{d2} = 0$, $\gamma_1 = \gamma_2 = 0$, $C_{L0} = 0.28$, $F = 1.2534e^{-2}$, $G = 0.3763$, $\lambda = 0.9988$, $\bar{\mu} = 0.002$, and $\sigma = -0.1$. (Color figure online)

absorber and vortex shedding. From Fig. 6, it can be observed that as the value of σ approaches 0, the steady-state response of the wake variable also increases and becomes maximum at the first critical value of σ . However, a further increase in the value of σ decreases the value of the steady-state response, and at the second critical value of σ , there is a sudden drop in the value. Also, as the value of σ increases further, the steady-state response increases and attains a constant value.

To further demonstrate the effect of the wake variable on the system dynamics, we compare the frequency response of the system with lift force modeled as a wake oscillator and sinusoidal lift-force. To achieve this, it is necessary to establish the similarities between both models. Hence, we substitute the value of stall term, i.e., α , as 0 in the governing equations so that the only sources of damping in the system are realized through structural damping and damping in vibration absorber. Also, the excitation amplitude used in [21] is amplified by the average of the steady-state response of wake variable q_y over the frequency range. With these values of stall parameter and excitation amplitude, the frequency-response curve is analyzed and shown in Fig. 7(i). In Fig. 7, the solid

curve represents stable branch of solutions, whereas dashed line represents unstable branch of solutions. From Fig. 7(i), it can be observed that for the given value of primary system parameters, i.e., for cable-absorber system, the sinusoidal lift-force model overestimates the maximum amplitude as compared to wake oscillator model. To further demonstrate the effect of the wake variable on the system dynamics, we compare the frequency response curves corresponding to a sinusoidal model amplified by maximum value (Max. Sinusoidal model) and minimum value (Min. Sinusoidal model) of the wake variable with the frequency response curve corresponding to the wake oscillator model as shown in Fig. 7(ii). The results show a significant difference between the maximum amplitude of steady-state response due to the variation in q_y . Further, it can be observed that the maximum value of steady state response corresponding to Min. Sinusoidal model is approximately equivalent to the one corresponding to the wake oscillator model; however, it does not capture the effect of nonlinearity in the system. These observation can be explained through the significant variation of the steady-state response of wake variable q_y near $\sigma = 0$. The sudden decrease in the steady-

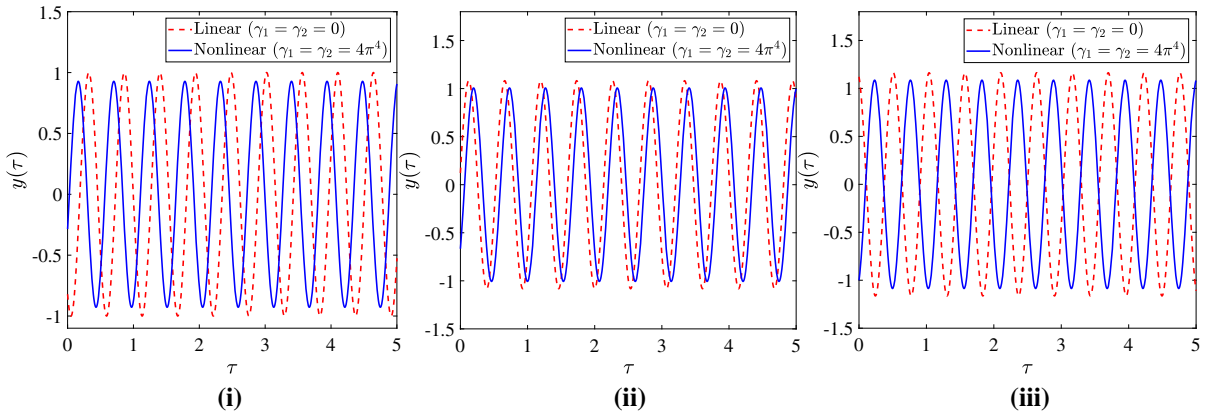


Fig. 5 Comparison of time response of the system with and without nonlinearity in vibration absorber for (i) $\epsilon^2\sigma = -0.1$, (ii) $\epsilon^2\sigma = 0$, and $\epsilon^2\sigma = 0.1$. The other system parameters are $\xi_1 = 0.1$, $\xi_2 = 0.9$, $\alpha_{11} = \alpha_{12} = .01$, $\alpha_{21} = \alpha_{22} = .2$, $k_{11} = k_{12} =$

$2\pi^4$, $s = 2$, $f_L = 20$, $\alpha = 0.01$, $c_{d1} = c_{d2} = 0$, $\gamma_1 = \gamma_2 = 0$, $C_{L0} = 0.28$, $F = 1.2534e^{-2}$, $G = 0.3763$, $\lambda = 0.9988$, and $\bar{\mu} = 0.002$. (Color figure online)

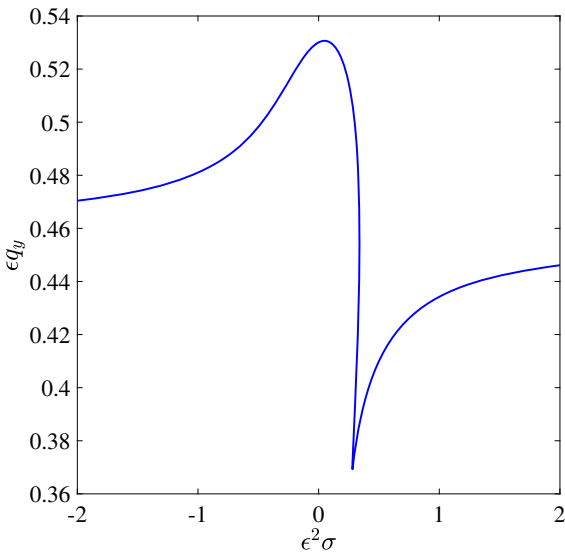


Fig. 6 Frequency response of the wake variable for $\epsilon = 0.01$. The other system parameters are $\xi_1 = 0.1$, $\xi_2 = 0.9$, $\alpha_{11} = \alpha_{12} = .01$, $\alpha_{21} = \alpha_{22} = 0.2$; $k_{11} = k_{12} = \pi^4/2.5$, $s = 2$, $f_L^* = 1000$, $\alpha = 0$, $c_{d1}^* = c_{d2}^* = 30$, $\gamma_1 = k_{11}/2$, $\gamma_2 = k_{11}/2$, $C_{L0}^* = 28$, $F^* = 1.2534e^2$, $G = 0.3763$, $\lambda = 0.9988$, and $\bar{\mu}^* = 0.2$. (Color figure online)

state response of q_y around σ_0 causes decrease in the effective amplitude of excitation, which further causes decrease in the steady-state response of the primary system, i.e., a_y .

Having established the difference between the current model and that of [21], next the effect of different

system and fluid parameters on the system’s dynamics through frequency response curves is presented. For the sake of simplicity of analysis, we consider the case of cable/conductor with two vibration absorbers placed at both ends of the cable. Also due to the symmetrical boundary conditions for the cable, variation in either absorber’s parameters will have the same effect on system dynamics. Therefore, in the current analysis the parameters corresponding to the vibration absorbers are varied simultaneously. We first examine the effect of nonlinear stiffness of the vibration absorber on the system dynamics. This step also acts to establish the effectiveness of the nonlinear vibration absorber over the linear vibration absorber. Figure 8 depicts the variation of frequency response curves for the different values of γ_{1p} . The frequency response curve corresponding to $\gamma_{11} = \gamma_{12} = 0$ represents the case of linear vibration absorber, whereas the frequency response curves corresponding to $\gamma_{11} \neq 0$, $\gamma_{12} \neq 0$ represent the case of nonlinear vibration absorber. From Fig. 8, it can be observed that increase in the nonlinear stiffness slightly decreases the maximum value of steady-state response of the cable. Additionally, when increasing the nonlinear stiffness, the effective bandwidth of the nonlinear absorber increases, which further implies an increase in the operating range of the vibration absorber. For the sake of completeness, we also compare the dynamics of a system with nonlinear vibration absorber (NVA) and nonlinear energy sink (NES) which is shown in Fig. 9. For the case of a nonlinear energy sink, the

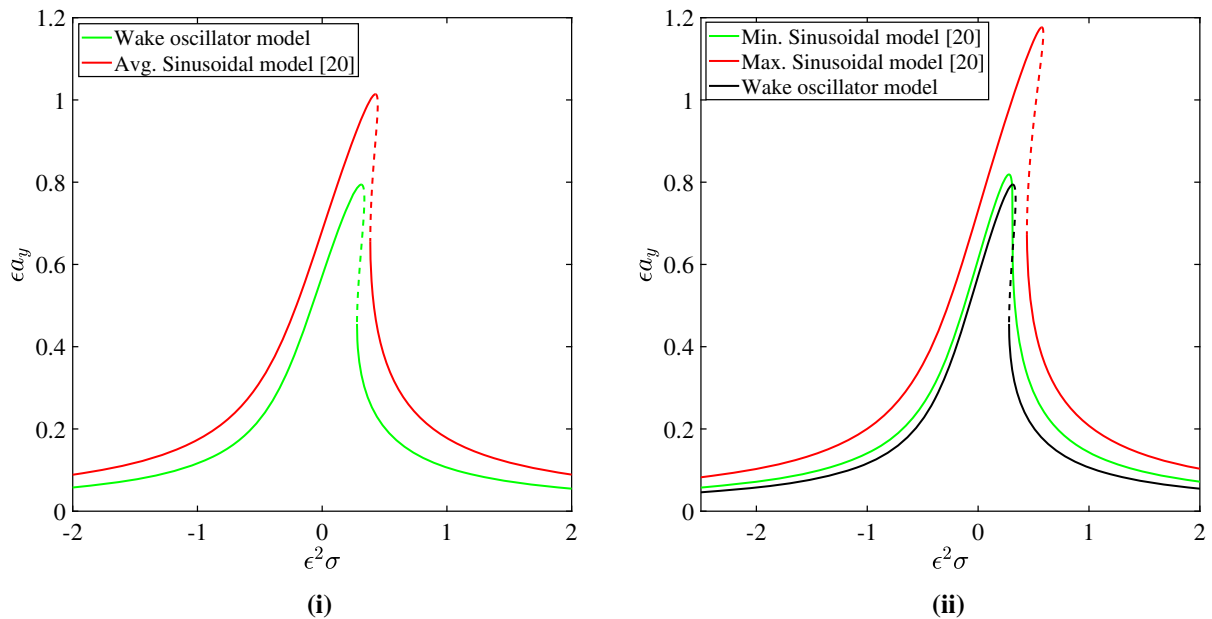


Fig. 7 (i) Comparison of the frequency response of the cable with wake oscillator and sinusoidal force corresponding average value of q_y , and (ii) frequency response curves for sinusoidal force with maximum and minimum value of q_y for $\epsilon = 0.01$. The other system parameters are $\xi_1 = 0.1$, $\xi_2 = 0.9$, $\alpha_{11} =$

$\alpha_{12} = .01$, $\alpha_{21} = \alpha_{22} = 0.2$, $k_{11} = k_{12} = \pi^4/2.5$, $s = 2$, $f_L^* = 1000$, $\alpha = 0$, $c_{d1}^* = c_{d2}^* = 30$, $\gamma_1 = k_{11}/2$, $\gamma_2 = k_{11}/2$, $C_{L0}^* = 28$, $F^* = 1.2534e^2$, $G = 0.3763$, $\lambda = 0.9988$, and $\bar{\mu}^* = 0.2$. (Color figure online)

nonlinear vibration absorber does not have any linear stiffness and hence, does not have any natural frequency. This fact further implies a larger bandwidth for the nonlinear energy sink at the cost of higher amplitude of steady-state response of the cable as shown in Fig. 9. Also, from Fig. 9 we observe a very sharp change in the frequency-response curve (marked by circle) corresponding to NES. This sharp change in the frequency response curve is attributed to a small value of stall parameter in the system. We emphasize that this link between value of stall parameter and sharp change in frequency-response curve depends on the parameter values of the primary system. Therefore, this sharp change does not appear in the frequency response curve corresponding to NVA for the same value of stall parameter, i.e., $\alpha = 0.01$.

Figure 10 shows the variation of frequency response curves for the different values of suspended mass in vibration absorbers with and without damping. From Fig. 10(i), it can be observed that as the value of suspended mass increases, the maximum amplitude of the cable's steady state response decreases. Also, the effect of nonlinearity becomes less evident with higher values

of suspended mass and eventually decreases the effective bandwidth of nonlinear vibration absorber. However, from Fig. 10(ii), it can be observed that without any damping in the absorber, the maximum amplitude of steady state response increases with increasing suspended mass. We emphasize that both of these observations are consistent with the observations drawn in [21]. Further, the effect of the absorber's in-span mass on system dynamics is shown in Fig. 11. Contrary to the observations drawn for the suspended mass, the maximum amplitude of the steady-state response of the cable increases slowly with increase in α_{1p} and the bandwidth remains ineffective with change in in-span mass. This observation can be attributed to the fact that the in-span mass oscillates with the same frequency and amplitude as the cable at the absorber location. Hence, it does not contribute significantly in the vibration absorption. Therefore, from Figs. 10 and 11 it can be concluded that for the given parameters of the primary system and wake oscillator, a nonlinear vibration absorber performs better with increase in the suspended mass at the cost of a decrease in bandwidth.

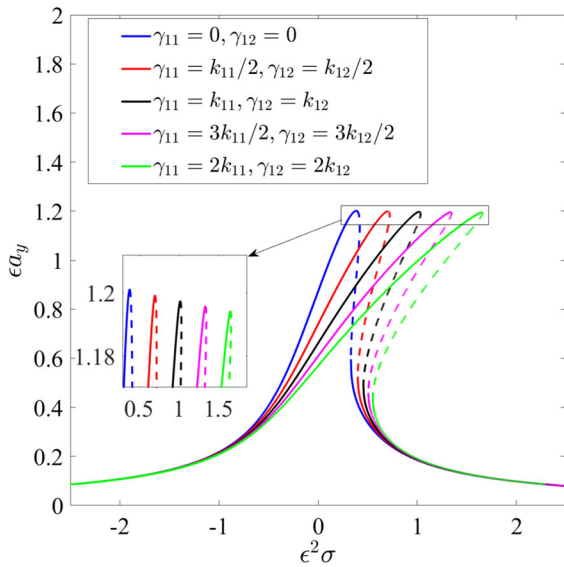


Fig. 8 Comparison of the frequency response curves for linear vibration absorber ($\gamma_{1p} = 0$) with nonlinear vibration absorber ($\gamma_{1p} \neq 0$) $\epsilon = 0.01$. The other system parameters are $\xi_1 = 0.1, \xi_2 = 0.9, \alpha_{11} = \alpha_{12} = .01, \alpha_{21} = \alpha_{22} = 0.2, k_{11} = k_{12} = \pi^4/2.5, s = 2, f_L^* = 2000, \alpha = 0.01, c_{d1}^* = c_{d2}^* = 30, C_{L0}^* = 28, F^* = 1.2534e^2, G = 0.3763, \lambda = 0.9988,$ and $\bar{\mu}^* = 0.2$. (Color figure online)

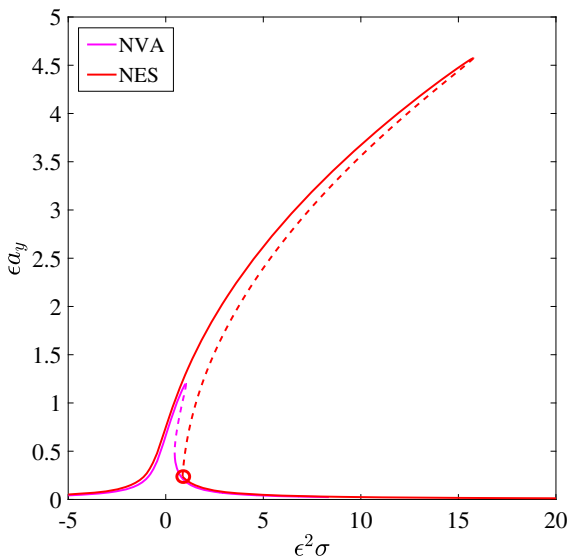


Fig. 9 Comparison of frequency response curves corresponding to nonlinear vibration absorber and nonlinear energy sink shown by Magenta and Red colors, respectively, with $\epsilon = 0.01$. The other system parameters are $\xi_1 = 0.1, \xi_2 = 0.9, \alpha_{11} = \alpha_{12} = .01, \alpha_{21} = \alpha_{22} = 0.2; k_{11} = k_{12} = \pi^4/2.5, s = 2, f_L^* = 2000, \alpha = 0.01, \gamma_1 = k_{11}, \gamma_2 = k_{11}, c_{d1}^* = c_{d2}^* = 30, C_{L0}^* = 28, F^* = 1.2534e^2, G = 0.3763, \lambda = 0.9988,$ and $\bar{\mu}^* = 0.2$. (Color figure online)

Figures 12 and 13 show the variation of frequency response curves with damping of the cable and linear stiffness of the nonlinear absorbers, respectively. From Fig. 12, it can be observed that for the given values of cable and wake oscillator parameters, high values of damping reduce the maximum value of steady-state response of the cable, but decrease the effective nonlinearity in the system and eventually reduce the bandwidth of the nonlinear absorber. Also, after a certain value of damping, the system begins behaving like a linear system for the given value of excitation amplitude. Contrary to the effect of damping, the absorber’s linear stiffness has an opposite effect on system’s dynamics. From Fig. 13, it can be observed that for given system parameters, increase in k_{p1} not only increases the maximum amplitude, but also increases the effective nonlinearity in the system, hence increasing the bandwidth for the nonlinear vibration absorber.

Having established the effect of absorber properties on the system dynamics, the effect of the absorber location on the frequency response curves is presented next. Figure 14 shows the variation of frequency response curves with absorber location. From Fig. 14, colored it can be observed that as the absorbers move toward the midpoint of the cable from both sides, the maximum value of steady-state response of the cable decreases, as does the effect of nonlinearity in the system. However, close to the midpoint of the cable, the system dynamics get saturated as both absorbers together act as one equivalent absorber placed at the center of cable.

Next, the effect of cable and wake oscillator parameters on the dynamics of the system is presented. Figure 15 depicts the effect of variation in s , which quantifies the tension in the cable, on the frequency response of the cable. From Fig. 15, it can be observed that higher values of s not only reduce the maximum amplitude of steady-state response of the cable, but also the effective nonlinearity in the system and eventually the effective bandwidth of the nonlinear absorber. After a critical value of s , the system tends to become more linear and nonlinearity in the system is not evident at all. This observation can be explained through the fact that a low value of s signifies slack cables, which are more susceptible to high-amplitude low-frequency vibrations than highly stretched cables. However, highly stretched cables are subjected to high-frequency low-amplitude vibrations, which lead to fatigue failure of the cable. Hence, there is a restriction on the value of axial tension T and eventually on s . Figures 16

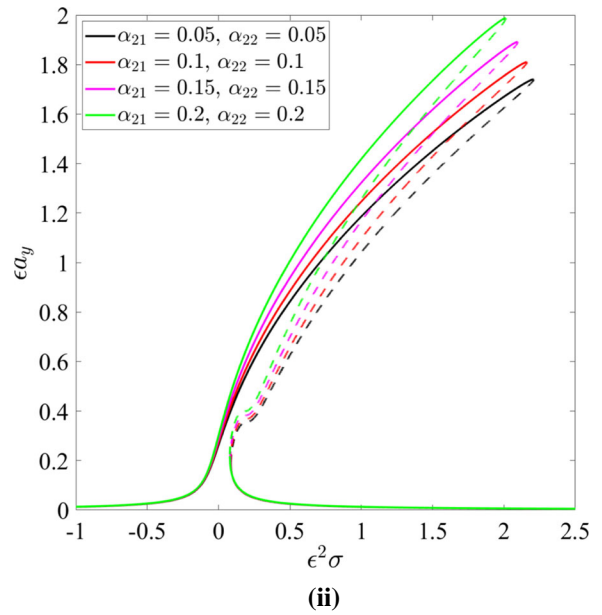
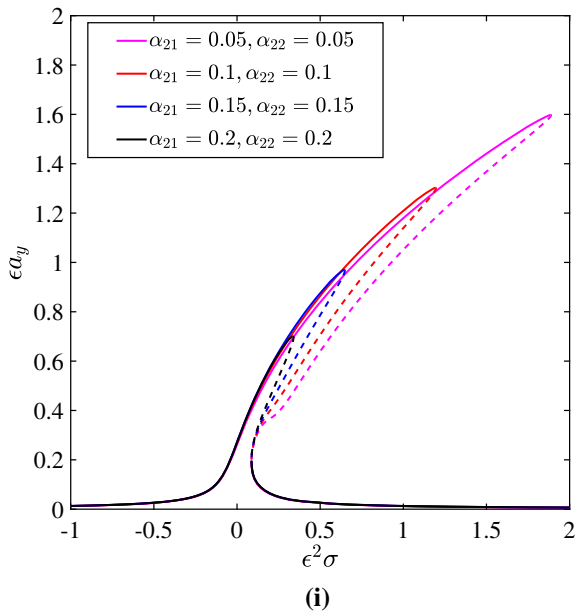


Fig. 10 Frequency response curves for different values of suspended mass with $\epsilon = 0.01$ (i) with $c_{dp}^* \neq 0$, and (ii) with $c_{dp}^* = 0$. The other system parameters are $\xi_1 = 0.1$, $\xi_2 = 0.9$, $\alpha_{11} = \alpha_{12} = .01$, $k_{11} = k_{12} = \pi^4$, $s = 2$, $f_L^* = 100$, $\alpha = 0.1$, $c_{d1}^* =$

$c_{d2}^* = 30$, $\gamma_1 = k_{11}/2$, $\gamma_2 = k_{11}/2$, $C_{L0}^* = 28$, $F^* = 1.2534e^3$, $G = 0.3763$, $\lambda = 0.9988$, and $\bar{\mu}^* = 0.2$. (Color figure online)

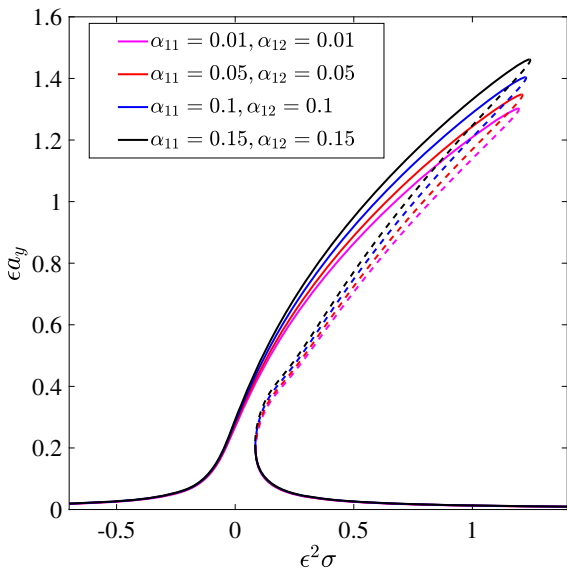


Fig. 11 Frequency response curves for different values of in-span mass with $\epsilon = 0.01$. The other system parameters are $\xi_1 = 0.1$, $\xi_2 = 0.9$, $\alpha_{21} = \alpha_{22} = .1$, $k_{11} = k_{12} = \pi^4$, $s = 2$, $f_L^* = 100$, $\alpha = 0.1$, $c_{d1}^* = c_{d2}^* = 30$, $\gamma_1 = k_{11}/2$, $\gamma_2 = k_{11}/2$, $C_{L0}^* = 28$, $F^* = 1.2534e^2$, $G = 0.3763$, $\lambda = 0.9988$, and $\bar{\mu}^* = 0.2$. (Color figure online)

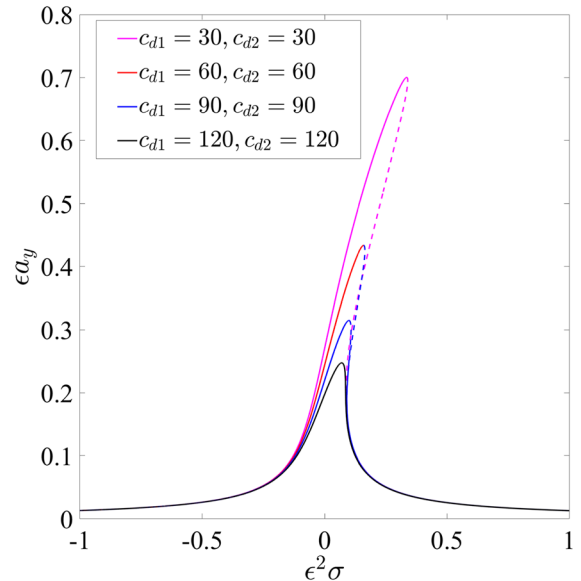


Fig. 12 Frequency response curves for different values of damping in absorber with $\epsilon = 0.01$. The other system parameters are $\xi_1 = 0.1$, $\xi_2 = 0.9$, $\alpha_{11} = \alpha_{12} = .01$, $\alpha_{21} = \alpha_{22} = 0.2$; $k_{11} = k_{12} = \pi^4$, $s = 2$, $f_L^* = 100$, $\alpha = 0.1$, $\gamma_1 = k_{11}/2$, $\gamma_2 = k_{11}/2$, $C_{L0}^* = 28$, $F^* = 1.2534e^2$, $G = 0.3763$, $\lambda = 0.9988$, and $\bar{\mu}^* = 0.2$. (Color figure online)

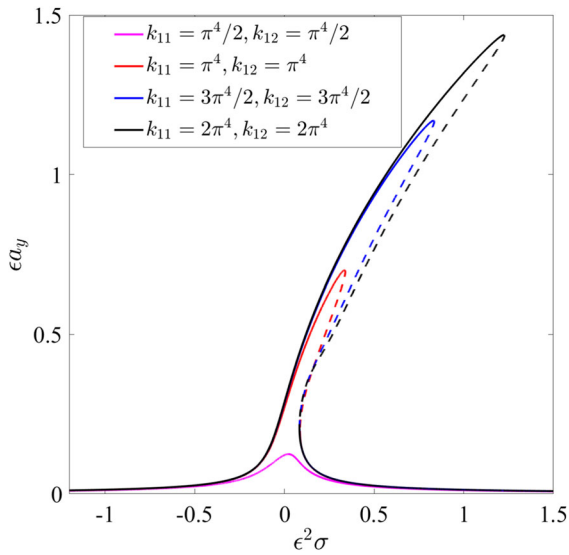


Fig. 13 Frequency response for different values of linear stiffness in absorber with $\epsilon = 0.01$. The other system parameters are $\xi_1 = 0.1, \xi_2 = 0.9, \alpha_{11} = \alpha_{12} = .01, \alpha_{21} = \alpha_{22} = 0.2, s = 2, f_L^* = 100, \alpha = 0.1, c_{d1}^* = c_{d2}^* = 30, \gamma_1 = \pi^4/2, \gamma_2 = \pi^4/2, C_{L0}^* = 28, F^* = 1.2534e^2, G = 0.3763, \lambda = 0.9988,$ and $\bar{\mu}^* = 0.2$. (Color figure online)

and 17 depict the effect of stall parameter (α) and damping coefficient in wake oscillator on the frequency response of the system, respectively. From Fig. 16, it can be observed that as the value of the stall parameter increases, the maximum amplitude of the steady-state response decreases along with the effective bandwidth of the nonlinear absorber. This observation for α can be attributed to the fact that increase in the value of α increases the effective damping of the system and therefore decreases the maximum amplitude of steady state response and nonlinearity. However, from Fig. 17 it can be observed that increasing the value of damping in wake oscillator decreases the maximum amplitude without any significant change in the effective bandwidth for the nonlinear absorber.

5 Conclusion

In this work, the nonlinear dynamics of an overhead transmission line system consisting of a single cable/conductor with multiple nonlinear vibration absorbers in the form of Stockbridge dampers was examined. The lift force was modeled as a wake oscillator in the form of a Van der Pol oscillator instead

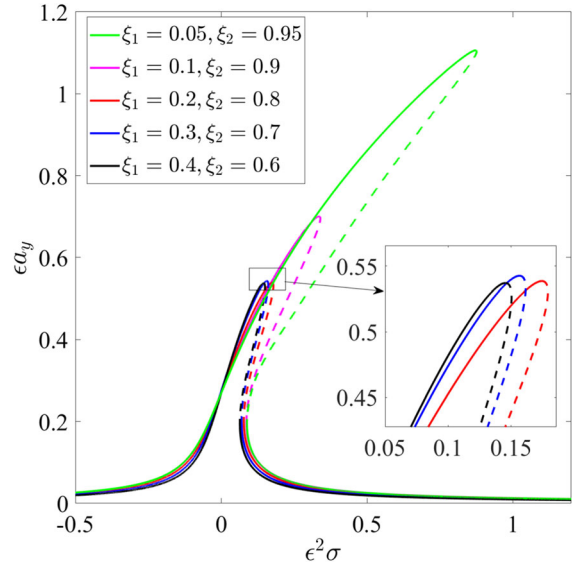


Fig. 14 Frequency response for different absorber locations with $\epsilon = 0.01$. The other system parameters are $\alpha_{11} = \alpha_{12} = .01, \alpha_{21} = \alpha_{22} = 0.2, s = 2, f_L^* = 100, \alpha = 0.1, c_{d1}^* = c_{d2}^* = 30, k_{11} = k_{12} = \pi^4, \gamma_1 = \pi^4/2, \gamma_2 = \pi^4/2, C_{L0}^* = 28, F^* = 1.2534e^2, G = 0.3763, \lambda = 0.9988,$ and $\bar{\mu}^* = 0.2$. (Color figure online)

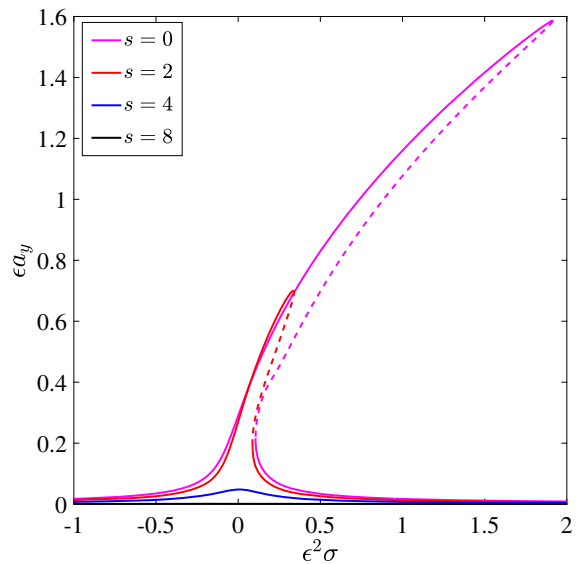


Fig. 15 Frequency response for different values of tension with $\epsilon = 0.01$. The other system parameters are $\xi_1 = 0.1, \xi_2 = 0.9, \alpha_{11} = \alpha_{12} = .01, \alpha_{21} = \alpha_{22} = 0.2, f_L^* = 100, \alpha = 0.1, c_{d1}^* = c_{d2}^* = 30, k_{11} = k_{12} = \pi^4, \gamma_1 = \pi^4/2, \gamma_2 = \pi^4/2, C_{L0}^* = 28, F^* = 1.2534e^2, G = 0.3763, \lambda = 0.9988,$ and $\bar{\mu}^* = 0.2$. (Color figure online)

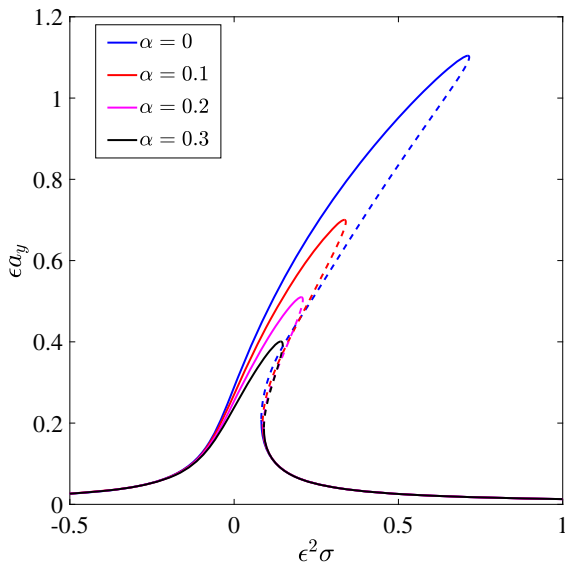


Fig. 16 Frequency response for different values of stall parameter with $\epsilon = 0.01$. The other system parameters are $\xi_1 = 0.1$, $\xi_2 = 0.9$, $\alpha_{11} = \alpha_{12} = .01$, $\alpha_{21} = \alpha_{22} = 0.2$, $f_L^* = 100$, $s = 2$, $c_{d1}^* = c_{d2}^* = 30$, $k_{11} = k_{12} = \pi^4$, $\gamma_1 = \pi^4/2$, $\gamma_2 = \pi^4/2$, $C_{L0}^* = 28$, $F^* = 1.2534e^2$, $G = 0.3763$, $\lambda = 0.9988$, and $\bar{\mu}^* = 0.2$. (Color figure online)

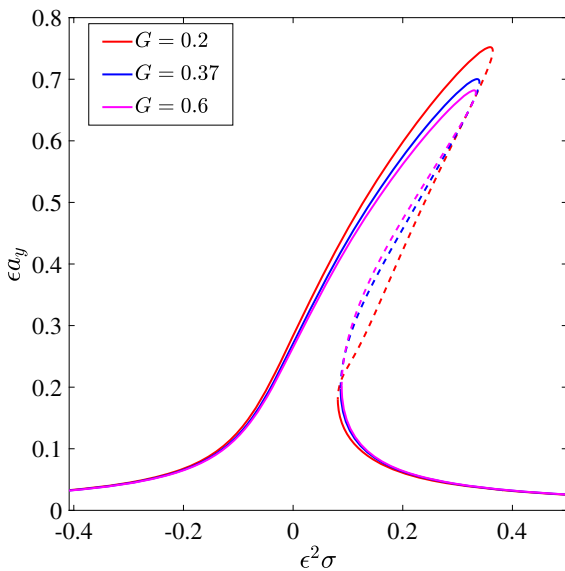


Fig. 17 Frequency response for different values of wake oscillator damping coefficient with $\epsilon = 0.01$. The other system parameters are $\xi_1 = 0.1$, $\xi_2 = 0.9$, $\alpha_{11} = \alpha_{12} = .01$, $\alpha_{21} = \alpha_{22} = 0.2$, $f_L^* = 100$, $s = 2$, $c_{d1}^* = c_{d2}^* = 30$, $k_{11} = k_{12} = \pi^4$, $\gamma_1 = \pi^4/2$, $\gamma_2 = \pi^4/2$, $C_{L0}^* = 28$, $F^* = 1.2534e^4$, $\alpha = 0.1$, $\lambda = 0.9988$, and $\bar{\mu}^* = 0.2$. (Color figure online)

of a traditional sinusoidal model. This step allowed us to consider nonlinearity in the lift force and was more realistic than a sinusoidal model. Furthermore, the cable/conductor was modeled as a simply supported beam, while the Stockbridge dampers were modeled as lumped mass–spring–damper–mass systems. The nonlinearity in the system was realized not only through the mid-plane stretching of the cable, but also through the equivalent cubic nonlinearity of the Stockbridge dampers. Linear and nonlinear analytical study of the coupled system of nonlinear partial differential equations, i.e., the equations of motion governing the response of the cable along with the equation governing the lift coefficient, were carried out using the method of multiple scales. Accordingly, the equations governing the steady-state response of the cable for the case of lock-in phenomenon were obtained and solved numerically. For numerical validation of the obtained analytical solutions, a reduced-order system was developed using Galerkin projection of the governing partial differential equations. The solution was then validated against direct numerical simulations of the reduced-order system and the results showed very good agreement. The response of the cable with wake oscillator was also compared to the response of the cable with sinusoidal lift force. We observed interesting dynamics of the wake variable around the zero value of the detuning parameter, which further contributes to the correct evaluation of system dynamics near resonance. We also observed that modeling lift force as sinusoidal overestimates the maximum value of steady-state response. Finally, a parametric study was carried out to identify key system parameters. It was observed that increasing the suspended mass and damping of the Stockbridge damper decreases the maximum value of steady-state response of the cable at the cost of reduction in the effective bandwidth of the nonlinear absorber. Also, it was observed that the in-span mass of the absorber does not influence the dynamics of the system significantly. A comparison between linear and nonlinear vibration absorbers revealed that the effective bandwidth of a nonlinear vibration absorber increases with increasing nonlinear stiffness without significantly affecting the maximum value of steady-state response of the cable. We further observed that locating absorbers near the ends of the cable results in increased effective bandwidth, while locating them closer to the middle results in smaller steady-state amplitude. We also analyzed the effect of axial tension and stall parameter of the wake

oscillator on the system dynamics. The results indicated that nonlinearity in the system vanishes with increase in the values of these parameters.

Acknowledgements This work was funded by National Science Foundation CAREER Award ECCS #1944032. Any opinions, findings, and conclusions or recommendations expressed in this material are those of the author(s) and do not necessarily reflect the views of the National Science Foundation.

Compliance with ethical standards

Conflict of interest The authors declare that they have no conflict of interest.

Appendix A: Expressions used in Eq. (34)

For the sake of simplicity, slow flow equations (Eq (33)), governing the amplitude and phase, can be written in a more compact form as

$$D_2 a_y = A_{11} + B_{11} \sin(\Gamma), \tag{39a}$$

$$D_2 q_y = A_{12} + B_{12} \cos(\Gamma), \tag{39b}$$

$$D_2 \Gamma = \sigma + B_{14} \sin(\Gamma) - A_{13} - B_{13} \cos(\Gamma), \tag{39c}$$

where A_{ij} (for $i = 1, 2, 3$ and $j = 1, 2, 3$) and B_{ij} (for $i = 1, 2, 3$ and $j = 1, 2, 3, 4$) are the function of system parameters, excitation frequency, and amplitudes a_y and q_y . These are given by

$$A_{11} = \frac{\sum_{p=1}^n [a_y c_{dp} (\Psi_p - 1) Y_p(\xi_p)^2 + a_y k_p \Psi_{4,p} (1 - \Psi_p) Y_p(\xi_p)]}{\sum_{p=1}^n [k_p Y_p(\xi_p) \Psi_{3,p} + 2 Y_p(\xi_p)^2 \alpha_{1p}] + 2b_1} - \frac{2\omega_y a_y f_L^* \bar{\alpha} b_1 + 2\omega_y a_y \bar{\mu} b_1 \omega_s}{\sum_{p=1}^n [\omega_s \omega_y k_p Y_p(\xi_p) \Psi_{3,p} + 2\omega_s \omega_y Y_p(\xi_p)^2 \alpha_{1p}] + 2\omega_y \omega_s b_1} \tag{40a}$$

$$B_{11} = \frac{f_L^* q_y b_1 \omega_s}{\sum_{p=1}^n [\omega_s \omega_y k_p Y_p(\xi_p) \Psi_{3,p} + 2\omega_s \omega_y Y_p(\xi_p)^2 \alpha_{1p}] + 2\omega_y \omega_s b_1} \tag{40b}$$

$$A_{12} = \omega_s G C_{L0}^* q_y b_1 - q_y^3 G \omega_s b_{12}, \quad B_{12} = \frac{1}{2b_1} a_y F^* \omega_y b_1, \tag{40c}$$

$$A_{13} = \frac{\sum_{p=1}^n (6a_y^3 k_p Y_p(\xi_p) \Psi_{2,p} - 6a_y^3 \gamma_p Y_p(\xi_p)^4 \Psi_{1,p})}{\sum_{p=1}^n a_y \omega_y [16b_1 + 8k_p Y_p(\xi_p) \Psi_{3,p} + 16Y_p(\xi_p)^2 \alpha_{1p}]} - \frac{3a_y^3 \lambda b_2 b_3}{\sum_{p=1}^n a_y \omega_y [16b_1 + 8k_p Y_p(\xi_p) \Psi_{3,p} + 16Y_p(\xi_p)^2 \alpha_{1p}]} \tag{40d}$$

$$B_{13} = \frac{-8 f_L^* q_y b_1}{\sum_{p=1}^n a_y \omega_y [16b_1 + 8k_p Y_p(\xi_p) \Psi_{3,p} + 16Y_p(\xi_p)^2 \alpha_{1p}]},$$

$$B_{14} = -\frac{1}{2q_y} a_y F^* \omega_y. \tag{40e}$$

As mentioned in the main text, the steady state amplitudes and phase can be obtained by setting $D_2 a_y = D_2 q_y = D_2 \Gamma = 0$, which further leads to

$$A_{11}^* + B_{11}^* \sin(\Gamma^*) = 0, \tag{41a}$$

$$A_{12}^* + B_{12}^* \cos(\Gamma^*) = 0, \tag{41b}$$

$$\sigma + B_{14}^* \sin(\Gamma^*) - A_{13}^* - B_{13}^* \cos(\Gamma^*) = 0. \tag{41c}$$

In the above equation, superscript * refers to steady state quantities. Equations (41a) and (41b) can be solved for $\sin(\Gamma^*)$ and $\cos(\Gamma^*)$ to get

$$\sin(\Gamma^*) = -\frac{A_{11}^*}{B_{11}^*}, \quad \cos(\Gamma^*) = -\frac{A_{12}^*}{B_{12}^*}. \tag{42}$$

In the next step, by using trigonometric identity, and substituting Eq. (42) in Eq. (41c), we get two algebraic equations in the form of

$$\left(\frac{A_{11}^*}{B_{11}^*}\right)^2 + \left(\frac{A_{12}^*}{B_{12}^*}\right)^2 - 1 = 0, \tag{43a}$$

$$\sigma - B_{14}^* \frac{A_{11}^*}{B_{11}^*} - A_{13}^* + B_{13}^* \frac{A_{12}^*}{B_{12}^*} = 0, \tag{43b}$$

Note that in the above equations except a_y^* and q_y^* all the system and excitation parameters are known, hence, these simultaneous algebraic equations can be used to govern the steady state amplitudes a_y^* and q_y^* and can be written in a compact form as

$$G_1(a_y^*, q_y^*) = \left(\frac{A_{11}^*}{B_{11}^*}\right)^2 + \left(\frac{A_{12}^*}{B_{12}^*}\right)^2 - 1 = 0 \tag{44}$$

$$G_2(a_y^*, q_y^*) = \sigma - B_{14}^* \frac{A_{11}^*}{B_{11}^*} - A_{13}^* + B_{13}^* \frac{A_{12}^*}{B_{12}^*} = 0.$$

References

1. Skop, R.A., Balasubramanian, S.: A new twist on an old model for vortex-excited vibrations. *J. Fluids Struct.* **11**(4), 395–412 (1997)
2. Benedettini, F., Rega, G.: Non-linear dynamics of an elastic cable under planar excitation. *Int. J. Non-Linear Mech.* **22**(6), 497–509 (1987)
3. Chan, J., et al.: *EPR Transmission Line Reference Book: Wind-Induced Conductor Motion*. Electric Power Research Institute, Palo Alto, CA (2009)
4. Barry, O., Zu, J.W., Oguamanam, D.C.D.: Analytical and experimental investigation of overhead transmission line vibration. *J. Vib. Control* **21**(14), 2825–2837 (2015)
5. Barry, O., Oguamanam, D.C., Lin, D.C.: Aeolian vibration of a single conductor with a stockbridge damper. In *Proceedings of the Institution of Mechanical Engineers, Part C: Journal of Mechanical Engineering Science*, pp. 935–945. Institution of Mechanical Engineers (2013)
6. Barry, O., Long, R., Oguamanam, D.C.: Simplified vibration model and analysis of a single-conductor transmission line with dampers. In: *Proceedings of the Institution of Mechanical Engineers, Part C: Journal of Mechanical Engineering*

- Science, Vol. 231, pp. 4150–4162. Institution of Mechanical Engineers, New York (2016)
7. Barry, O., Zu, J.W., Oguamanam, D.C.D.: Forced vibration of overhead transmission line: analytical and experimental investigation. *J. Vib. Acoust.* **136**, 4 (2014)
 8. Oliveira, A.R.E., Freire, D.G.: Dynamical modelling and analysis of aeolian vibrations of single conductors. *IEEE Trans. Power Deliv.* **9**(3), 1685–1693 (1994)
 9. Verma, H., Hagedorn, P.: Wind induced vibrations of long electrical overhead transmission line spans: a modified approach. *Wind Struct.* **8**(2), 89–106 (2005)
 10. Schäfer, B.: Dynamical modelling of wind-induced vibrations of overhead lines. *Int. J. Non-Linear Mech.* **19**(5), 455–467 (1984)
 11. Kraus, M., Hagedorn, P.: Aeolian vibrations: wind energy input evaluated from measurements on an energized transmission line. *IEEE Trans. Power Deliv.* **6**(3), 1264–1270 (1991)
 12. Nigol, O., Houston, H.J.: Aeolian vibration of single conductor and its control. *IEEE Trans. Power Deliv.* **104**(11), 3245–3254 (1985)
 13. Tompkins, J.S., Merrill, L.L., Jones, B.L.: Quantitative relationships in conductor vibration using rigid models. *IEEE Trans. Power Appar. Syst.* **75**(11), 879–894 (1956)
 14. Rawlins, C.B.: Recent developments in conductor vibration. Alcoa Technical Paper No. 13 (1958)
 15. Hardy, C., Noiseux, D.U.: Modeling of a Single Conductor-Damper System Response, vol 1. Theoretical and Validation Manual. CEA, Hydro (1996)
 16. Noiseux, D.U., Hardy, C., Houle, S.: Statistical methods applied to aeolian vibration of overhead conductors. *J. Sound Vib.* **113**(2), 245–255 (1987)
 17. Tsui, Y.T.: Recent advances in engineering science as applied to aeolian vibrations an alternative approach. *Electr. Power Syst. Res.* **5**, 73–85 (1982)
 18. Dowell, E.H.: Component mode analysis of nonlinear and nonconservative systems. *J. Appl. Mech.* **47**(1), 172–176 (1980)
 19. Pakdemirli, M., Nayfeh, A.H.: Nonlinear vibrations of a beam-spring-mass system. *J. Vib. Acoust.* **116**(4), 433–439 (1994)
 20. Barry, O., Oguamanam, D.C.D., Zu, J.W.: Nonlinear vibration of an axially loaded beam carrying multiple mass-spring-damper systems. *Nonlinear Dyn.* **77**, 1597–1608 (2014)
 21. Bukhari, M., Barry, O.: Nonlinear vibrations analysis of overhead power lines: a beam with mass-spring-damper-mass systems. *J. Vib. Acoust.* **140**(3) (2017)
 22. Khan, N.S., Islam, S., Gul, T., Khan, W., Khan, I., Ali, L., Khan, N., Waris, K., Als, L.: Thin film flow of a second grade fluid in a porous medium past a stretching sheet with heat transfer. *Alexandria Eng. J.* **57**, 1019–1031 (2017)
 23. Khan, N.S., Gul, T., Islam, S., Khan, I., Alqahtani, A.M., Alshomrani, A.S.: Magneto hydrodynamic nanoliquid thin film sprayed on a stretching cylinder with heat transfer. *Appl. Sci.* **7**, 271 (2017)
 24. Khan, I., Shafie, S.: Rotating mhd flow of a generalized burgers' fluid over an oscillating plate embedded in a porous medium. *Thermal Sci.* **19**, 183–190 (2015)
 25. Zuhra, S., Khan, N.S., Khan, M., Islam, S., Khan, W., Bonyah, E.: Flow and heat transfer in water based liquid film fluids dispensed with graphene nanoparticles. *Results Phys.* **8**, 1143–1157 (2018)
 26. Khan, N.S., Gul, T., Khan, M.A., Bonyah, E., Islam, S.: Mixed convection in gravity-driven thin film non-newtonian nanofluids flow with gyrotactic microorganisms. *Results Phys.* **7**, 4033–4049 (2017)
 27. Morkovin, M.V.: Flow around circular cylinders. a calescope of challenging fluid phenomena. In: ASME Symposium on Fully Separated Flows, Philadelphia, PA, pp. 102–118 (1964)
 28. Marris, A.W.: A review on vortex streets, periodic wakes, and induced vibration phenomena. *ASME J. Basic Eng.* **86**, 185–196 (1964)
 29. Mair, W.A., Maull, D.J.: Bluff bodies and vortex shedding—a report on euromech 17. *J. Fluid Mech.* **45**, 209–224 (1971)
 30. Hartlen, R.T., Currie, I.G.: Lift-oscillator model of vortex-induced vibration. *J. Eng. Mech. Div.* **96**(5), 577–591 (1970)
 31. Skop, R.A., Griffin, O.M.: A model for the vortex-excited resonant response of bluff cylinders. *J. Sound Vib.* **27**(2), 225–233 (1973)
 32. Iwan, W.D., Blevins, R.D.: A model for vortex induced oscillation of structures. *J. Appl. Mech.* **41**(3), 581–586 (1974)
 33. Skop, R.A., Griffin, O.M.: On a theory for the vortex-excited oscillations of flexible cylindrical structures. *J. Sound Vib.* **41**, 263–274 (1974)
 34. Iwan, W.D.: The vortex induced oscillation of elastic structural elements. *ASME J. Eng. Ind.* **97**, 1378–1382 (1975)
 35. Williamson, C.H.K., Govardhan, R.: Vortex-induced vibrations. *Annu. Rev. Fluid Mech.* **36**, 413–455 (2004)
 36. Kim, W.-J., Perkins, N.C.: Two-dimensional vortex-induced vibration of cable suspensions. *J. Fluids Struct.* **16**(2), 229–245 (2002)
 37. Facchinetti, M.L., de Langre, E., Biolley, F.: Coupling of structure and wake oscillators in vortex-induced vibrations. *J. Fluids Struct.* **19**(3), 123–140 (2004)
 38. Govardhan, R., Williamson, C.H.K.: Modes of vortex formation and frequency response of a freely vibrating cylinder. *J. Fluid Mech.* **420**, 85130 (2000)
 39. Norberg, C.: Fluctuating lift on a circular cylinder: review and new measurements. *J. Fluids Struct.* **17**(1), 57–96 (2003)
 40. Sarpakaya, T.: Vortex-induced oscillations: a selective review. *J. Appl. Mech.* **46**, 241–258 (1979)
 41. Griffin, O.M., Ramberg, S.E.: Some recent studies of vortex shedding with application to marine tubulars and risers. *ASME J. Energy Resour. Technol.* **104**, 2–13 (1982)
 42. Parkinson, G.: Phenomena and modeling of flow-induced vibrations of bluff bodies. *Prog. Aerosp. Sci.* **26**, 169–224 (1989)
 43. Pantazopoulos, M.S.: Vortex-induced vibration parameters: critical review. *Proc. Int. Conf. Offshore Mech. Arct. Eng.* **1**, 199–255 (1994)
 44. Nayfeh, A.H., Mook, D.T.: *Nonlinear Oscillations*. Wiley, New York (2008)
 45. Wu, J.-S., Chou, H.-M.: Free vibration analysis of a cantilever beam carrying any number of elastically mounted point masses with the analytical-and-numerical-combined method. *J. Sound Vib.* **213**(2), 317–332 (1998)
 46. Ramberg, S.E., Griffin, O.M.: Vortex formation in the wake of a vibrating, flexible cable. *ASME J. Fluids Eng.* **96**, 317–322 (1974)

47. Ramberg, S.E., Griffin, O.M.: Velocity correlation and vortex spacing in the wake of a vibrating cable. *ASME J. Fluids Eng.* **99**, 10–18 (1976)
48. Nayfeh, A.H.: *Introduction to Perturbation Techniques*. Wiley, New York (1981)

Publisher's Note Springer Nature remains neutral with regard to jurisdictional claims in published maps and institutional affiliations.